

1 **MESMO 3: Flexible phytoplankton stoichiometry and refractory DOM**

2

3 **Katsumi Matsumoto, Tatsuro Tanioka<sup>+</sup>, and Jacob Zahn**

4

5 Department of Earth & Environmental Sciences, University of Minnesota, Minneapolis,  
6 Minnesota, USA

7 <sup>+</sup> Current affiliation: Department of Earth System Science, University of California Irvine,  
8 Irvine, California, USA

9

10 Contact: katsumi@umn.edu

11

12 (revised version submitted 3/18/2021 to *Geoscientific Model Development*)

13

14 **Abstract**

15 We describe the third version of Minnesota Earth System Model for Ocean biogeochemistry  
16 (MESMO 3), an earth system model of intermediate complexity, with a dynamical ocean, a  
17 dynamic-thermodynamic sea ice, and an energy moisture balanced atmosphere. A major  
18 feature of Version 3 is the flexible C:N:P ratio for the three phytoplankton functional types  
19 represented in the model. The flexible stoichiometry is based on the power law formulation  
20 with environmental dependence on phosphate, nitrate, temperature, and light. Other new  
21 features include nitrogen fixation, water column denitrification, oxygen and temperature-  
22 dependent organic matter remineralization, and  $\text{CaCO}_3$  production based on the concept of  
23 the residual nitrate potential growth. Also, we describe the semi-labile and refractory  
24 dissolved organic pools of C, N, P, and Fe that can be enabled in MEMSO 3 as an optional  
25 feature. The refractory dissolved organic matter can be degraded by photodegradation at  
26 the surface and hydrothermal vent degradation at the bottom. These improvements  
27 provide a basis for using MESMO 3 in further investigations of the global marine carbon  
28 cycle to changes in the environmental conditions of the past, present, and future.

29

## 30 **1. Introduction**

31 Here we document the development of the third version of the Minnesota Earth System  
32 Model for Ocean biogeochemistry (MESMO 3). As described for the first two versions  
33 (Matsumoto et al., 2008, 2013), MESMO is based on the non-modular version of the Grid  
34 ENabled Integrated Earth (GENIE) system model (Lenton et al., 2006; Ridgwell et al., 2007).  
35 The computationally efficient ocean-climate model of Edwards and Marsh (Edwards and  
36 Marsh, 2005) forms the core of GENIE's physical model. MESMO is an earth system model  
37 of intermediate complexity (EMIC), which occupies a midpoint in the continuum of climate  
38 models that span high resolution, comprehensive coupled models on one end and box  
39 models at the other end (Claussen et al., 2002). MESMO has a 3D dynamical ocean model on  
40 a 36 x 36 equal-area horizontal grid with 10° increments in longitude and uniform in the  
41 sine of latitude. There are 16 vertical levels. It is coupled to a 2D energy moisture balanced  
42 model of the atmosphere and a 2D dynamic and thermodynamic model of sea ice. Thus,  
43 MESMO retains important dynamics, which allow for simulations of transient climate  
44 change, while still being computationally efficient.

45  
46 Since the first version, MESMO has continued to be developed chiefly for investigations of  
47 ocean biogeochemistry (Table 1). Briefly, in MESMO 1, the main improvements over the  
48 predecessor GENIE focused on the biological production and remineralization as well as on  
49 the uptake of natural radiocarbon ( $^{14}\text{C}$ ) and anthropogenic transient tracers (Matsumoto et  
50 al., 2008). The net primary production (NPP) in MESMO 1 occurred in the top two vertical  
51 levels representing the surface 100 m and depended on temperature, nutrients, light, and  
52 mixed layer depth (MLD). The nutrient dependence was based on the Michaelis-Menten  
53 uptake kinetics of phosphate ( $\text{PO}_4$ ), nitrate ( $\text{NO}_3$ ), and aqueous  $\text{CO}_2$ . The limiting nutrient  
54 was determined by the Liebig's rule of the minimum relative to the fixed uptake  
55 stoichiometry of C:N:P=117:16:1. A single generic phytoplankton functional type (PFT)  
56 carried out NPP, which was split between particulate organic matter (POM) and dissolved  
57 organic matter (DOM) in a globally constant ratio of 1:2. The semi-labile form of the  
58 dissolved organic carbon (DOC) was the only form of DOM simulated in MESMO 1. The POM  
59 flux across the 100 m level defined the export production. The vertical flux of POM was

60 driven by a fixed rate of sinking and a temperature-dependent, variable remineralization  
61 rate.

62  
63 The main aim of MESMO 2 was a credible representation of the marine silica cycle  
64 (Matsumoto et al., 2013). To this end, the set of limiting nutrients (P, N, and C) in MESMO 1  
65 was augmented to include iron (Fe) and silicic acid ( $\text{Si(OH)}_4$ ) in MESMO 2 (Table 1). The  
66 stable isotope of Si ( $^{30}\text{Si}$ ) was also added as a state variable. The Fe cycle included an  
67 aeolian flux of Fe, complexation with organic ligand, and particle scavenging of free Fe. The  
68 scavenged Fe that reached the seafloor was removed from the model domain. This burial  
69 flux of Fe balanced the aeolian flux at steady state. Also, a new PFT was added in MESMO 2  
70 to represent chiefly diatoms. This new "large" PFT was limited by Si and characterized by a  
71 high maximum growth rate and large half-saturation constants for the nutrient uptake  
72 kinetics. It represented fast and opportunistic phytoplankton that do well under nutrient  
73 replete conditions. In comparison, the "small" PFT was characterized with a lower  
74 maximum growth rate and smaller half-saturation constants and outperformed the large  
75 PFT in oligotrophic subtropical gyres.  $\text{CaCO}_3$  production was associated with the "small"  
76 PFT in MESMO2. The addition of Fe, Si, and the large PFT in MESMO 2 allowed it to have a  
77 Fe-dependent, variable Si:N uptake ratio (Hutchins and Bruland, 1998; Takeda, 1998),  
78 which is critical to simulate important features of the global ocean Si distribution.

79  
80 MESMO 1 and 2 were assessed and calibrated by multi-objective tuning and extensive  
81 model-data comparisons of transient tracers (anthropogenic carbon, CFCs), deep ocean  
82  $\Delta^{14}\text{C}$ , and nutrients (Matsumoto et al., 2008, 2013). These versions have been employed  
83 successfully in a number of studies of global distributions of carbon and carbon isotopes  
84 under various conditions of the past, present, and future (Cheng et al., 2018; Lee et al.,  
85 2011; Matsumoto et al., 2010, 2020; Matsumoto and McNeil, 2012; Matsumoto and  
86 Yokoyama, 2013; Sun and Matsumoto, 2010; Tanioka and Matsumoto, 2017; Ushie and  
87 Matsumoto, 2012). Also, MESMO 1 and 2 have participated in model intercomparison  
88 projects (Archer et al., 2009; Cao et al., 2009; Eby et al., 2013; Joos et al., 2013; Weaver et  
89 al., 2012; Zickfeld et al., 2013).

90  
91 In this contribution, we describe the third and latest version of MEMSO with a number of  
92 substantial biogeochemical model modifications and new features that bring MESMO up to  
93 date with the evolving and accumulating knowledge of the ocean biogeochemical cycle  
94 (Table 1). There is no change in the physical model between MESMO 3 and MESMO 2. The  
95 most significant new feature of MESMO 3 over the previous versions is the power law  
96 formulation of flexible phytoplankton C:N:P ratio. Other new features include additional  
97 PFT diazotrophs that carry out N-fixation, water column denitrification, the dependence of  
98 organic matter remineralization on the dissolved oxygen ( $O_2$ ) and temperature, and  $CaCO_3$   
99 production based on the concept of the residual nitrate potential growth. Also, we describe  
100 the semi-labile DOM for P, N, and Fe ( $DOP_{sl}$ ,  $DON_{sl}$ , and  $DOFe_{sl}$ ), and the refractory DOM for  
101 C, P, and N ( $DOC_r$ ,  $DOP_r$ , and  $DON_r$ ), which can be activated as an optional feature in MESMO  
102 3. Some of these features have been described separately in different publications  
103 (Matsumoto et al., 2020; Matsumoto and Tanioka, 2020; Tanioka and Matsumoto, 2017,  
104 2020a). This work consolidates the descriptions of all these features in a single publication.

105

## 106 **2. Model Description**

107 Here we present the full set of biogeochemical equations of MESMO 3 as well as key model  
108 parameters (Table 2). We describe only the biogeochemical source and sink terms and omit  
109 the physical (advective and diffusive) transport terms that are calculated by the ocean  
110 circulation model. We discuss the production terms first, followed by remineralization  
111 terms, followed by conservation equations that incorporate both terms.

112

### 113 **2.1 Phytoplankton Nutrient Uptake**

114 NPP occurs in the top two vertical levels of the ocean domain above the fixed compensation  
115 depth ( $z_c$ ) of 100 m. Key parameter values are given in Table 2a. Nutrient uptake by  
116 phytoplankton type  $i$  ( $\Gamma_i$ ) depends on the optimal nutrient uptake timescale ( $\tau_i$ ), nutrients,  
117 temperature ( $T$ ), irradiance ( $I$ ), and mixed layer depth ( $z_{ml}$ ):

118

$$\Gamma_i = \frac{1}{\tau_i} \cdot F_{N,i} \cdot F_T \cdot F_I \cdot \max \left\{ 1, \frac{Z_c}{Z_{ml}} \right\} \quad 1$$

119

120 Subscript i refers to PFT (i =1: eukaryotes, i =2: cyanobacteria, i = 3: diazotrophs). The  
 121 nutrient dependence  $F_{N,i}$  is given by Liebig's law of minimum combined with Michael-  
 122 Menten uptake kinetics of limiting nutrients:  $PO_4$ ,  $NO_3$ ,  $CO_2$ , (aq), total dissolved iron (sum  
 123 of free iron and ligand-bound iron;  $FeT=Fe'+FeL$ ), and silicic acid ( $Si(OH)_4$ ):

124

$$F_{N,i} = \min \left( \frac{[PO_4]}{[PO_4]+K_{PO_4,i}} \cdot [PO_4], \frac{[NO_3]}{[NO_3]+K_{NO_3,i}} \cdot [NO_3] \cdot Q_{N,i}^{-1}, \frac{[CO_2(aq)]}{[CO_2(aq)]+K_{CO_2,i}} \cdot [CO_2(aq)] \cdot Q_{C,i}^{-1}, \frac{[FeT]}{[FeT]+K_{FeT,i}} \cdot [FeT] \cdot Q_{Fe,i}^{-1}, \frac{[Si(OH)_4]}{[Si(OH)_4]+K_{Si(OH)_4}} \cdot [Si(OH)_4] \cdot Q_{Si}^{-1} \right), \quad 2$$

125

126 where  $K_{X,i}$  is the half-saturation concentration of nutrient X for PFT i. Only eukaryotes (i=1)  
 127 are limited by  $Si(OH)_4$ . Diazotrophs (i = 3) are not limited by  $NO_3$ . Nutrient uptake  $\Gamma$  is  
 128 based on the master nutrient variable P, and all other nutrient uptake is related to  $\Gamma$  by the  
 129 uptake stoichiometry  $Q_{X,i}$ , where X is N, Fe, Si, or C. For example,  $Q_{C,i} = \frac{1}{[P:C]_i}$  for PFT i. Thus,  
 130  $Q_{C,i}$  is numerically equivalent to C:P for PFT i, but we write the equations in terms of P:C for  
 131 numerical stability and convenience. The  $Q_{X,i}$  ratios represent the flexible phytoplankton  
 132 uptake stoichiometry and describe more fully in the following section 2.2.

133

134 The temperature dependence  $F_T$  of Equation 1 is given by:

135

$$F_T = \frac{T(^{\circ}C) + 2}{T(^{\circ}C) + 10} \quad 3$$

136

137 which is analogous to the commonly used  $Q_{10} = 2$  relationship. Light limitation  $F_I$  of  
 138 Equation 1 is described by a hyperbolic function:

$$F_T = \frac{I}{I + 20}$$

4

139

140 where  $I$  is the seasonally variable solar short-wave irradiance in  $\text{W m}^{-2}$ . Light is attenuated  
141 exponentially from the ocean surface with a 20 m depth scale.

142

143 Nutrient uptake in Equation 1 has a dependence on  $z_{ml}$ , which is diagnosed using the  $\sigma_t$   
144 density gradient criterion (Levitus, 1982). Following the Sverdrup (1953) model of the  
145 spring bloom, Equation 1 allows for the shoaling of  $z_{ml}$  relative to  $z_c$  to enhance nutrient  
146 uptake.

147

## 148 **2.2 Phytoplankton uptake stoichiometry**

149 As noted above, all nutrients and  $\text{O}_2$  are related to the main model currency  $P$  by  $Q_{X,i}$ . We  
150 describe three different, mutually exclusive formulations in this section. The standard  
151 formulation is the power law model (Matsumoto et al., 2020; Tanioka and Matsumoto,  
152 2017). The other two (Linear model and Optimality-based model of stoichiometry) are  
153 alternative formulations that have been coded, and the user can activate them (one at a  
154 time) in place of the power law formulation. However, the alternative formulations are not  
155 calibrated. Key parameter values are given in Table 2b for the power law formulation.

156

### 157 **2.2.1 Power law model of stoichiometry**

158 The uptake P:C and N:C ratios are calculated using the power-law formulation as a function  
159 of ambient concentrations of phosphate [ $\text{PO}_4$ ], nitrate [ $\text{NO}_3$ ], temperature ( $T$ ), and  
160 Irradiance ( $I$ ):

161

$$[P:C]_i = [P:C]_{0,i} \cdot \left(\frac{[PO_4]}{[PO_4]_0}\right)^{s_{PO_4,i}^{P:C}} \cdot \left(\frac{[NO_3]}{[NO_3]_0}\right)^{s_{NO_3,i}^{P:C}} \cdot \left(\frac{T}{T_0}\right)^{s_{T,i}^{P:C}} \cdot \left(\frac{I}{I_0}\right)^{s_{I,i}^{P:C}} \quad 5$$

$$[N:C]_i = [N:C]_{0,i} \cdot \left(\frac{[PO_4]}{[PO_4]_0}\right)^{s_{PO_4,i}^{N:C}} \cdot \left(\frac{[NO_3]}{[NO_3]_0}\right)^{s_{NO_3,i}^{N:C}} \cdot \left(\frac{T}{T_0}\right)^{s_{T,i}^{N:C}} \cdot \left(\frac{I}{I_0}\right)^{s_{I,i}^{N:C}} \quad 6$$

162

163 Equations 5 and 6 are the power-law equations that calculate the change in P:C and N:C for  
 164 fractional changes in environmental drivers relative to the reference P:C and N:C,  
 165 respectively (Matsumoto et al., 2020; Tanioka and Matsumoto, 2017). The exponents are  
 166 the sensitivity factors determined by a meta-analysis (Tanioka and Matsumoto, 2020a).  
 167 Subscript "0" indicates the reference values (Table 2b). We have hard bounds for the  
 168 calculated P:C and N:C ratios to be within  $26.6 < C:P < 546.7$  and  $2 < C:N < 30$  as observed  
 169 (Martiny et al., 2013).

170

171 The P:C and N:C ratios from Equations 5 and 6 can then be converted to  $Q_{N,i}$  and  $Q_{C,i}$  for use  
 172 in Equation 2.

173

$$Q_{C,i} = \frac{1}{[P:C]_i} \quad 7$$

$$Q_{N,i} = \frac{1}{[P:N]_i} = \frac{[N:C]_i}{[P:C]_i} \quad 8$$

174

### 175 **2.2.2 Linear model of stoichiometry by Galbraith & Martiny**

176 A much simpler, alternative formulation for P:C and N:C is the model of Galbraith & Martiny  
 177 (2015) where P:C is a linear function of  $[PO_4]$  (in  $\mu M$ ), and N:C is a Holling type 2 functional  
 178 form with a frugality behavior only at very low  $[NO_3]$  (in  $\mu M$ ). The same P:C and N:C values  
 179 are applied to all three PFTs.

180



$$[P:C] = \frac{6.9 \cdot [PO_4] + 6.0}{1000} \quad 9$$

$$[N:C] = 0.125 + \frac{0.03 \cdot [NO_3]}{0.32 + [NO_3]} \quad 10$$

181

### 182 **2.2.3 Optimality-based model of stoichiometry**

183 The optimality-based model of phytoplankton growth is based on the chain model, which  
 184 connects the cellular P, N, and C acquisition by a chain of limitations, where the P quota  
 185 limits N assimilation and the N quota drives carbon fixation (Pahlow et al., 2013; Pahlow  
 186 and Oschlies, 2009, 2013). Resource-allocation of cellular P, N, and C among different  
 187 cellular compartments are derived from balancing energy gain from gross carbon fixation  
 188 and energy loss due to nutrient acquisition and light-harvesting. The optimality-based  
 189 model by Pahlow et al. (2013) computes C:N and C:P as a function of nutrient availability  
 190 ( $PO_4$  and  $NO_3$ ), irradiance, and day length. Temperature dependence was added by  
 191 Arteaga et al. (2014) following the simple logarithmic temperature dependence on  
 192 maximum nutrient uptake rate following (Eppley, 1972).

193

194 Different versions of this optimality-based model have previously been successfully  
 195 implemented in global ocean biogeochemical models, such as the Pelagic Interactions  
 196 Scheme for Carbon and Ecosystem Studies (PISCES) (Kwiatkowski et al., 2018, 2019) and  
 197 the University of Victoria Earth System Model (UVIC) (Chien et al., 2020; Pahlow et al.,  
 198 2020). However, as we are not describing any results in this paper, we will only mention  
 199 here that there is an option to calculate C:N:P using this stoichiometry model in MESMO 3.  
 200 The full description of the optimality-based stoichiometry model and its parameter  
 201 calibration are presented specifically for the UVic model elsewhere (Chien et al., 2020;  
 202 Pahlow et al., 2020).

203

### 204 **2.2.4 Stoichiometry of iron and silica**

205 Iron uptake stoichiometry  $Q_{Fe,i}$  is calculated as a function of FeT following the power-law  
 206 formulation of Ridgwell (2001). Key parameter values are given in Table 2c.

207

$$Q_{Fe,i} = [Fe:P]_i = [Fe:C]_i \cdot Q_{C,i} \quad 11$$

$$[Fe:C]_i = 1.0 / ([C:Fe]_{min,i} + [C:Fe]_{ref,i} \cdot [FeT]^{-s^{Fe:C}_i}) \quad 12$$

208

209 For all PFTs, the power law exponent  $s^{Fe:C}$  in Equation 12 is -0.65. The allowable Fe:C ratio  
 210 is bounded at the low end by the hard-bound minimum Fe:C of 1:220,000. The scaling  
 211 constant or  $[C:Fe]_{ref,i}$  is set differently for PFTs, with eukaryotes having a higher base  
 212  $[C:Fe]_{ref,i}$  than cyanobacteria and diazotrophs (115,623:1 and 31,805:1, respectively). The  
 213 high end of the allowable Fe:C ratio is bounded by  $[C:Fe]_{min,i}$  (i.e., maximum Fe:C) of  
 214 15,000:1 for eukaryotes and 20,000:1 for cyanobacteria/diazotrophs. These parameters  
 215 directly follow Ridgwell (2001), who fitted power-law functions to the experimental data  
 216 (Sunda and Huntsman, 1995).

217

218 Silica uptake stoichiometry by eukaryotes  $Q_{Si}$  is a power law of total dissolved iron [FeT]  
 219 and increases with a decrease in [FeT] (Brzezinski, 2002). The power law exponent  $s^{Si:N}$  is  
 220 set to 0.7. The Si:N ratio is limited to a maximum of 18 and a minimum of 1.

221

$$Q_{Si} = [Si:P] = [Si:N] \cdot Q_{N,1} \quad 13$$

$$[Si:N] = \min \left( [Si:N]_{max}, \max \left( [Si:N]_{min}, \left( \frac{[FeT]}{0.5 \text{ nmol kg}^{-1}} \right)^{-s^{Si:N}} \right) \right) \quad 14$$

222

223  $O_2$  liberated by phytoplankton during photosynthesis per  $PO_4$  consumed ( $Q_{-O_2,i}$ ) is  
 224 calculated from the uptake C:P and N:P ratios (Tanioka and Matsumoto, 2020b):

225

$$Q_{-O_2,i} = 1.1Q_{C,i} + 2Q_{N,i} \quad 15$$

226

### 227 **2.3 Production of POM and DOM**

228 In the top 100 m of the model domain, where phytoplankton P uptake occurs (i.e.,  $\Gamma_i > 0$ ,  
 229 see section 2.1), NPP is immediately routed to POM and DOM pools (Figure 1). The  
 230 production fluxes of POM,  $DOM_{sl}$ , and  $DOM_r$  from NPP are given as  $J_{prod}$ . Here we write the  
 231 equations in terms of P, which is the master nutrient variable:

$$J_{prod_{POM}} = (1 - fDOM) \cdot \Gamma_i \quad 16$$

$$J_{prod_{DOM_{sl}}} = \sum_i (1 - fDOM_r) \cdot fDOM \cdot \Gamma_i \quad 17$$

$$J_{prod_{DOM_r}} = \sum_i fDOM_r \cdot fDOM \cdot \Gamma_i \quad 18$$

233  
 234 The term  $fDOM$  denotes the fraction of NPP that is routed to DOM as opposed to POM.  
 235 Likewise,  $fDOM_r$  is the fraction of DOM that is routed to  $DOM_r$  as opposed to  $DOM_{sl}$ . The  
 236 value of  $fDOM_r$  is not well known but estimated to be  $\sim 1\%$  (Hansell, 2013), which we  
 237 tentatively adopt in MESMO 3. If  $DOM_r$  is not selected in the model run,  $fDOM_r = 0$ . In  
 238 previous versions of MESMO,  $fDOM$  was assigned a constant value of 0.67. In reality, a large  
 239 variability is observed locally for this ratio, ranging from 0.01-0.2 in temperate waters to  
 240 0.1-0.7 in the Southern Ocean (Dunne et al., 2005; Henson et al., 2011; Laws et al., 2000). In  
 241 MESMO 3,  $fDOM$  is calculated as a function of the ambient temperature following Laws et  
 242 al. (Laws et al., 2000):

$$fDOM = 1.0 - \min(0.72, \max(0.04, 0.62 - 0.02 \cdot T(^{\circ}C))) \quad 19$$

244  
 245 This formulation gives low export efficiency (i.e., high  $fDOM$ ) in the warmer regions  
 246 compared to the colder high latitude regions. Locally, we impose fixed  $fDOM$  upper and  
 247 lower bounds of 0.96 and 0.28, respectively, as estimated from a previous study (Dunne et  
 248 al., 2005).

249

250 In MEMSO 3, a new DOM production pathway below the production layer is available as an  
 251 option. In previous MESMO versions, sinking POM was respired in the water column with  
 252 the loss of O<sub>2</sub> directly to the dissolved inorganic forms (i.e., POC-->DIC, POP-->PO<sub>4</sub>, and  
 253 POP-->NO<sub>3</sub>). In the new "deep POC split" pathway, sinking POM is simply broken down into  
 254 DOM without the loss of O<sub>2</sub> as in the production layer (Figure 1). If DOM<sub>r</sub> is selected in the  
 255 model, the broken-down POM is further routed to both DOM<sub>sl</sub> and DOM<sub>r</sub> according to  
 256 fDOM<sub>r</sub>. If not, all of the broken down POM is converted to DOM<sub>sl</sub>. Thus, when the deep POC  
 257 split is activated, the presence of DOM in the deep ocean can be accounted for by *in situ*  
 258 production of DOM and DOM<sub>r</sub> in addition to DOM transport from the surface. Thus, the  
 259 deep POC split pathway offers an alternative means to control deep ocean DOM  
 260 distribution.

261

#### 262 **2.4 Production of CaCO<sub>3</sub> and opal by eukaryotes**

263 In MEMSO 2, opal production was associated with the large PFT and CaCO<sub>3</sub> production was  
 264 associated with the "small" PFT. We recognize that coccolithophorids and diatoms, which  
 265 are the producers of these biogenic tests, are both eukaryotes. Therefore, in MEMSO 3, we  
 266 associate both CaCO<sub>3</sub> and opal production with the POM production by the same eukaryote  
 267 PFT ( $J_{prod_{POM1}}$ ):

268

$$J_{prod_{CaCO_3}} = r^{CaCO_3:POC} \cdot J_{prod_{POM1}} \cdot Q_{C,1} \quad 20$$

$$J_{prod_{opal}} = J_{prod_{POM1}} \cdot Q_{Si} \quad 21$$

269

270 The concept of the residual nitrate potential growth (RNPG) (Balch et al., 2016) is useful in  
 271 allowing competition between diatoms and non-siliceous phytoplankton within the same  
 272 PFT (Matsumoto et al., 2020). Typically, in the real ocean, non-Si phytoplankton are able to  
 273 grow faster and dominate the community if Si concentration is low and diatom growth is Si  
 274 limited. Otherwise, diatoms are more competitive, as they have higher intrinsic growth  
 275 rates. The RNPG index recasts the ambient concentrations of NO<sub>3</sub> and Si(OH)<sub>4</sub> into potential  
 276 algal growth rates:

277

$$RNPG = \frac{[NO_3]}{[NO_3] + K_{NO_3,1}} - \frac{[Si(OH)_4]}{[Si(OH)_4] + K_{Si(OH)_4}} \quad 22$$

278

279 If RNPG is more positive, the index indicates that nitrate-dependent growth exceeds silica-  
 280 dependent growth. Thus, non-Si phytoplankton are more competitive, and this leads to  
 281 higher CaCO<sub>3</sub> production. On the other hand, a more negative RNPG implies that silica  
 282 limitation for diatoms is relieved, leading to enhanced diatom growth and reduced CaCO<sub>3</sub>  
 283 production. The RNPG index is incorporated in the calculation of the rain ratio  $r^{CaCO_3:POC}$   
 284 presented in Equation 20 as:

285

$$r^{CaCO_3:POC} = r_0^{CaCO_3:POC} \cdot (\Omega - 1)^\eta \cdot \min(1, \max(0.1, RNPG)) \cdot k_{T,CaCO_3} \quad 23$$

286

287 Equation 23 indicates the base rain ratio  $r_0^{CaCO_3:POC}$  (set to 0.30) is also modified by the  
 288 carbonate ion saturation state  $\Omega$  by  $\eta$  (set to 1.28) by as well as by temperature (see  
 289 Ridgwell et al. (2007) and references therein):

290

$$\Omega = \frac{[Ca^{2+}][CO_3^{2-}]}{K_{sp}} \quad 24$$

$$k_{T,CaCO_3} = \min\left(1.0, \frac{T(^{\circ}C) + 2}{T(^{\circ}C) + 8}\right) \quad 25$$

291

292  $K_{sp}$  is the solubility product of CaCO<sub>3</sub>. The temperature dependency of CaCO<sub>3</sub> formation  
 293 ( $k_{T,CaCO_3}$ ) is similar to that of Moore et al. (2004) where warmer temperatures favor the  
 294 growth of carbonate-bearing phytoplankton.

295

## 296 **2.5 Remineralization of POM and DOM**

297 Once produced, both POM and DOM undergo remineralization throughout the water  
 298 column. Key remineralization parameter values are given in Table 2d. Previously, POM

299 remineralization had a temperature dependence and decayed exponentially with depth  
300 (Yamanaka et al., 2004). In MESMO 3, we incorporate an additional dependency on  
301 dissolved oxygen following Laufkötter et al. (2017):

$$R_{POM_i} = V_{POM} \cdot e^{k_R \cdot T \cdot \frac{[O_2]}{[O_2] + K_{O_2}}} \cdot [POM_i] \quad 26$$

303  
304  $V_{POM}$  is the base remineralization rate, parameter  $k_R$  expresses the temperature sensitivity  
305 of remineralization, and  $K_{O_2}$  is half-saturation constant for oxygen-dependent  
306 remineralization. When the sediment model is not coupled, any POM that reaches the  
307 seafloor dissolves completely to its inorganic form and is returned to the overlying water.

308  
309 In MESMO 3, all forms of semi-labile DOM remineralize at the same rate. It is represented  
310 by  $\tau_{sl}$ , the inverse of the time scale of  $DOM_{sl}$  decay, which has been estimated previously to  
311 be  $\sim 1.5$  years (Hansell, 2013):

$$R_{DOM_{sl}} = \tau_{sl} \cdot [DOM_{sl}] \quad 27$$

313  
314 All forms of  $DOM_r$  also remineralize at the same rate in MESMO 3. In total, there are three  
315 optional, additive sinks of  $DOM_r$  in the model: slow background decay, photodegradation,  
316 and degradation via hydrothermal vents (Figure 1). Observations clearly indicate that the  
317  $^{14}C$  age of deep ocean  $DOC_r$  is  $10^3$  years (e.g., Druffel et al., 1992), much older than  $DI^{14}C$ .  
318 Also, the deep ocean  $DOC_r$  concentration decreases modestly along the path of the deep  
319 water from the deep North Atlantic to the deep North Pacific (Hansell and Carlson, 1998).  
320 Thus, it is understood that there is a slow  $DOM_r$  background decay in the deep ocean. We  
321 represent this ubiquitous process with  $\tau_{bg}$ , which is the inverse of the background decay  
322 time scale, estimated to be  $\sim 16,000$  years (Hansell, 2013).

323  
324 Observations to date indicate that photodegradation is a major sink of  $DOM_r$  (e.g., Mopper  
325 et al., 1991). This process is believed to convert  $DOM_r$  that is upwelled from the ocean

326 interior into the euphotic zone into more labile forms of DOM. We represent  
 327 photodegradation with  $\tau_{photo}$ , the inverse of the decay time scale, estimated to be  $\sim 70$  years  
 328 (Yamanaka and Tajika, 1997). This occurs only in the surface.

329  
 330 Finally, observations of DOM emanating from different types of hydrothermal vents  
 331 indicate that they have variable impacts on the deep sea  $DOM_r$  (Lang et al., 2006). However,  
 332 the off-axis vents circulate far more seawater through the fractured oceanic crust than the  
 333 high temperature and diffuse vents and thus believed to determine the overall impact of  
 334 the vents on the deep sea  $DOM_r$  as a net sink (Lang et al., 2006). Here we assume simply  
 335 that seawater that circulates through the vents loses all  $DOM_r$  (i.e.,  $1/\tau_{vent} \leq \Delta t$ , where  $\Delta t$  is  
 336 the biogeochemical model time step of 0.05 year). This means that the more seawater  
 337 circulates through the vents, the more  $DOM_r$  is removed: the total removal rate depends on  
 338 the vent flux of seawater  $H_{flux}$ . We implement the vent degradation of  $DOM_r$  in MESMO 3 by  
 339 first identifying the wet grid boxes located immediately above known mid-ocean ridges. We  
 340 then distribute the annual global  $H_{flux}$  of  $4.8 \times 10^{16}$  kg yr<sup>-1</sup> (Lang et al., 2006) equally among  
 341 those ridge-associated grid boxes. The grid cells contain a mass of seawater much greater  
 342 than the mass that circulates through vents in  $\Delta t$  ( $10^{21}$  kg vs.  $10^{13}$  kg). Therefore, the  
 343 seawater mass in the vent grid cells that does not circulate through the vents in  $\Delta t$  is  
 344 subject only to background degradation in MESMO 3.

345  
 346 The three  $DOM_r$  sinks are not mutually exclusive. They can thus be combined to yield the  
 347 total  $DOM_r$  remineralization rate:

$$R_{DOM_r} = (\tau_{bg} + \tau_{photo} + \tau_{vent} \cdot \frac{SW_{flux\_local}}{SW_{grid}}) \cdot [DOM_r] \quad 28$$

349  
 350 where  $SW_{flux\_local}$  is the mass of seawater that circulates through the vents in each grid box  
 351 in  $\Delta t$ , and  $SW_{grid}$  is the total mass of seawater in the same grid box.

352

353 The amount of O<sub>2</sub> respired as a result of these POM and DOM remineralization processes is  
354 related to the organic carbon pools by the respiratory quotients of POC and DOC,  $r_{-O_2:POC}$   
355 and  $r_{-O_2:DOC}$ , respectively. These are molar ratios of O<sub>2</sub> consumed per unit organic carbon  
356 respired. They are variable and calculated from the ambient POM and DOM concentration  
357 (Tanioka and Matsumoto, 2020b):

358

$$r_{-O_2:POC} = 1.1 + \frac{2[PON]}{[POC]} \quad 29$$

$$r_{-O_2:DOC} = 1.1 + \frac{2[DON]}{[DOC]} \quad 30$$

359

## 360 **2.6 Remineralization of CaCO<sub>3</sub> and opal**

361 Remineralization of CaCO<sub>3</sub> and opal particles occurs as they sink through the water column  
362 and remains the same as in MESMO 2. Key parameter values are given in Table 2d.

363 Remineralization of CaCO<sub>3</sub> is a function of temperature similar to that of particulate organic  
364 matter remineralization but without oxygen dependency. The temperature dependence  
365 term  $k_R$  modifies the base remineralization rate  $V_{CaCO_3}$ :

366

$$R_{CaCO_3} = V_{CaCO_3} \cdot e^{k_R T} \cdot [CaCO_3] \quad 31$$

367

368 Opal remineralization in the water column follows Ridgwell et al. (2002). The rate of opal  
369 remineralization  $R_{opal}$  is given by the product of normalized dissolution rate ( $r_{opal}$ ), base  
370 opal dissolution rate ( $k_{opal}$ ), and opal concentration [opal]:

371



$$R_{opal} = r_{opal} \cdot k_{opal} \cdot [opal] \quad 32$$

$$r_{opal} = 0.16 \cdot \left(1 + \frac{T(^{\circ}C)}{15}\right) \cdot u_{opal} + 0.55 \cdot \left(\left(1 + \frac{T(^{\circ}C)}{400}\right)^4 \cdot u_{opal}\right)^{9.25} \quad 33$$

$$u_{opal} = \frac{[Si(OH)_4]_{eq} - [Si(OH)_4]}{[Si(OH)_4]_{eq}} \quad 34$$

372

373  $r_{opal}$  is a function of temperature (T) and the degree of under-saturation ( $u_{opal}$ ), which in  
 374 turn is calculated from the ambient  $[Si(OH)_4]$  and  $[Si(OH)_4]$  at equilibrium. The  
 375 equilibrium concentration is a function of ambient temperature:

376

$$\log_{10}([Si(OH)_4]_{eq}) = 6.44 - \frac{968}{T(K)} \quad 35$$

377

378 Without the sediment module of MESMO activated, both  $CaCO_3$  and opal particles that  
 379 reach the seafloor are completely dissolved back to inorganic forms.

380

## 381 **2.7 Conservation of organic matter and biogenic tests**

382 The time rate of change of the biogenic organic matter and tests are given by the sum of the  
 383 production terms (i.e., sources) and the remineralization terms (i.e., sinks). The circulation-  
 384 related transport terms are omitted as noted above, but the vertical transport due to  
 385 particle sinking is included here. The sinking speed  $w$  is the same for all particles. The sum  
 386 of  $POM_i$  of all the PFTs give the total POM concentrations:

387

$$\frac{\partial[POP]_i}{\partial t} = Jprod_{POP_i} - \frac{\partial}{\partial Z}(w[POP]_i) - R_{POP,i} \quad 36$$

$$\frac{\partial[POC]_i}{\partial t} = Jprod_{POP_i} \cdot Q_{C,i} - \frac{\partial}{\partial Z}(w[POC]_i) - R_{POC,i} \quad 37$$

$$\frac{\partial[PON]_i}{\partial t} = Jprod_{POP_i} \cdot Q_{N,i} - \frac{\partial}{\partial Z}(w[PON]_i) - R_{PON,i} \quad 38$$

$$\frac{\partial[POFe]_i}{\partial t} = Jprod_{POP_i} \cdot Q_{Fe,i} - \frac{\partial}{\partial Z}(w[POFe]_i) - R_{POFe,i} \quad 39$$

$$[POM] = \sum_i [POM]_i \quad 40$$

388

389 The time rate of change of  $CaCO_3$  and opal is expressed in much the same way as POM:

390

$$\frac{\partial[CaCO_3]}{\partial t} = Jprod_{CaCO_3} - \frac{\partial}{\partial Z}(w[CaCO_3]) - R_{CaCO_3} \quad 41$$

$$\frac{\partial[opal]}{\partial t} = Jprod_{opal} - \frac{\partial}{\partial Z}(w[opal]) - R_{opal} \quad 42$$

391

392 The DOM pools have the production and remineralization terms without the particle  
393 sinking term:

394

$$\frac{\partial[DOP_{sl}]}{\partial t} = J_{prod_{DOP_{sl}}} - R_{DOP_{sl}} \quad 43$$

$$\frac{\partial[DON_{sl}]}{\partial t} = J_{prod_{DON_{sl}}} - R_{DON_{sl}} \quad 44$$

$$\frac{\partial[DOC_{sl}]}{\partial t} = J_{prod_{DOC_{sl}}} - R_{DOC_{sl}} \quad 45$$

$$\frac{\partial[DOFe_{sl}]}{\partial t} = J_{prod_{DOFe_{sl}}} - R_{DOFe_{sl}} \quad 46$$

$$\frac{\partial[DOP_r]}{\partial t} = J_{prod_{DOP_r}} - R_{DOP_r} \quad 47$$

$$\frac{\partial[DON_r]}{\partial t} = J_{prod_{DON_r}} - R_{DON_r} \quad 48$$

$$\frac{\partial[DOC_r]}{\partial t} = J_{prod_{DOC_r}} - R_{DOC_r} \quad 49$$

395

## 396 **2.8 Conservation of inorganic nutrients**

397 The time rate of change of the inorganic nutrients have organic carbon production as sink  
398 terms and remineralization as source terms. The production terms ( $J_{prod}$ ) are zero below  
399 the upper ocean production layer. Nutrients have a unit of mol element  $kg^{-1}$  in the model.

400

$$\frac{\partial[PO_4]}{\partial t} = - \sum_i \Gamma_i + \sum_i R_{POP,i} + R_{DOP_{sl}} + R_{DOP_r} \quad 50$$

$$\frac{\partial[NO_3]}{\partial t} = - \sum_i \Gamma_i \cdot Q_{N,i} + \sum_i R_{PON,i} + R_{DON_{sl}} + R_{DON_r} + Fix_N - Den_N \quad 51$$

$$\frac{\partial[DIC]}{\partial t} = - \left( \sum_i \Gamma_i Q_{C,i} + Jprod_{CaCO_3} \right) + \sum_i R_{POC,i} + R_{DOC_{sl}} + R_{DOC_r} + R_{CaCO_3} + F_{gas,CO_2} \quad 52$$

$$\frac{\partial[ALK]}{\partial t} = - \left( 2 \cdot Jprod_{CaCO_3} - \sum_i \Gamma_i Q_{N,i} \right) - \sum_i R_{PON,i} - R_{DON_{sl}} - R_{DON_r} - Fix_N + Den_N + 2 \cdot R_{CaCO_3} \quad 53$$

$$\frac{\partial[FeT]}{\partial t} = - \sum_i \Gamma_i Q_{Fe,i} + \sum_i R_{POFe,i} + R_{DOFe_{sl}} + R_{POM_{Fe}} + Aeolian_{Fe} \quad 54$$

$$\frac{\partial[Si(OH)_4]}{\partial t} = -Jprod_{opal} + R_{opal} \quad 55$$

$$\frac{\partial[O_2]}{\partial t} = \sum_i \Gamma_i \cdot Q_{-O_2,i} - \left( r_{-O_2:DOC} \cdot (R_{DOC_{sl}} + R_{DOC_r}) + \sum_i r_{-O_2:POC,i} \cdot R_{POC,i} \right) + 1.25 Den_N + F_{gas,O_2} \quad 56$$

401

402 In Equation 51,  $Fix_N$  is the N-fixation carried out by diazotrophs, and  $Den_N$  is the water  
 403 column denitrification. There is an air-sea gas exchange term  $F_{gas}$  in Equations 52 and 56 for  
 404 gaseous  $CO_2$  and  $O_2$ , respectively. In Equation 53, alkalinity increases with decreasing  
 405 nitrate concentrations and increasing  $CaCO_3$  dissolution. Equation 54 contains  $R_{POM_{Fe}}$ ,  
 406 which is an iron source that represents remineralization of the Fe' scavenged by sinking  
 407 particles. These terms are explained in the following sections.

408

409 **2.9 Prognostic nitrogen cycle**

410 Biological production by diazotrophs is stimulated when the ambient  $\text{NO}_3$  is low. Nitrogen  
 411 fixed by diazotrophs during their growth is added to the marine  $\text{NO}_3$  pool. The prognostic  
 412 nitrogen fixation model employed here is similar to that used in the HAMOCC  
 413 biogeochemical module (Paulsen et al., 2017):

414

$$Fix_N = \Gamma_3 \cdot Q_{N,3} \cdot I_{NO_3}, \quad 57$$

$$I_{NO_3} = \left( 1.0 - \frac{[NO_3]^2}{K_{N_2}^2 + [NO_3]^2} \right), \quad 58$$

415

416 where  $Fix_N$  is the nitrogen fixation rate and  $I_{NO_3}$  is the nitrate dependency term in  
 417 quadratic Michaelis-Menten kinetics form with the half-saturation constant  $K_{N_2}$ . See Table  
 418 2e for the values related to the N cycle.

419

420 Water-column denitrification is formulated in an approach similar to that of the original  
 421 GENIE model (Ridgwell et al., 2007), in which 2 moles of  $\text{NO}_3$  are converted to 1 mole of  $\text{N}_2$   
 422 and liberating 2.5 moles of  $\text{O}_2$  as a byproduct:

423



424

425 Denitrification takes place in grid boxes, in which  $\text{O}_2$  concentration is below a threshold  
 426 concentration ( $\text{O}_{2,\text{def}}$ ) and is stimulated if the total global inventory of  $\text{NO}_3$  relative to  $\text{PO}_4$  is  
 427 high. In other words, denitrification can effectively act as negative feedback to nitrogen  
 428 fixation. The threshold  $\text{O}_2$  concentration ( $\text{O}_{2,\text{def}}$ ) takes the minimum of the hard-bound  $\text{O}_2$   
 429 threshold concentration ( $\text{O}_{2,\text{crit}}$ ) and the  $\text{NO}_3$  to  $\text{PO}_4$  ratio, scaled by a parameter  $k_D$ . The  
 430 parameters  $\text{O}_{2,\text{crit}}$  and  $k_D$  are calibrated to give the global denitrification rate of roughly  
 431  $100 \text{ Tg N yr}^{-1}$ , which balances the total nitrogen fixation rate in the model.

432

$$Den_N = 0.8 \text{ [yr}^{-1}\text{]} \cdot \max\left(\left([O_2]_{def} - [O_2]\right), 0\right) \quad 60$$

$$[O_2]_{def} = \min\left(O_{2,crit}, k_D \cdot \frac{[NO_3]_{inventory}}{[PO_4]_{inventory}}\right) \quad 61$$

433

## 434 **2.10 Prognostic iron cycle**

435 The iron cycle in MESMO 3 remains the same as in MESMO 2. Key parameter values are  
 436 given in Table 2e. The two species of dissolved iron (Fe' and FeL) are partitioned according  
 437 to the following equilibrium relationship:

438

$$K_{ligand} = \frac{[FeL]}{[Fe'] \cdot [L]} \quad 62$$

439

440 where [L] is the ligand concentration, and  $K_{ligand}$  is the conditional stability constant. The  
 441 sum of ligand and FeL is set at a constant value of 1 nmol kg<sup>-1</sup> everywhere. Iron is  
 442 introduced into the model domain by a constant fraction (3.5 weight %) of aeolian dust  
 443 deposition at the surface ( $F_{in}$ ) following the prescribed modern flux pattern (Mahowald et  
 444 al., 2006) with constant solubility ( $\beta$ ):

445

$$S_{Fe} = \beta \cdot F_{in} \quad 63$$

446

447 Particle-scavenged iron  $POM_{Fe}$  (note the difference from  $PO_{Fe}$ ) is produced below the  
 448 productive layer when sinking POM scavenges Fe' to sinking POM:

449

$$J_{Fe} = -\tau_{sc} \cdot K_o \cdot [POC]^{0.58} \cdot [Fe'] \quad 64$$

450

451 where  $\tau_{sc}$  and  $K_o$  and are empirical parameters that determine the strength of scavenging.  
 452 Remineralization of Fe scavenged to POM ( $POM_{Fe}$ ) is identical in form to that of POM  
 453 remineralization:

454

$$R_{POM_{Fe}} = V_{POM} \cdot e^{k_{RT} \frac{[O_2]}{[O_2] + K_{O_2}}} \cdot [POM_{Fe}] \quad 65$$

455

456 The conservation equation of the particle scavenged iron is thus expressed as :

457

$$\frac{\partial [POM_{Fe}]}{\partial t} = J_{Fe} - \frac{\partial}{\partial z} (w [POM_{Fe}]) - R_{POM_{Fe}} \quad 66$$

458

459 Any scavenged iron that escapes remineralization in the water column reaching the  
460 seafloor is removed from the model domain in order to keep the total Fe inventory at a  
461 steady state.

462

### 463 **2.11 Air-sea gas Exchange**

464 The air-sea gas exchange formulation remains the same as in MESMO 2 and follows  
465 Ridgwell et al. (2007). It is the function of gas transfer velocity, the ambient dissolved gas  
466 concentration, and saturation gas concentration. The flux of CO<sub>2</sub> and O<sub>2</sub> gases across the  
467 air-sea interface is given by:

468

$$F_{gas,CO_2} = k \cdot ([CO_2]_{sat} - [CO_2]) \cdot (1 - A) \quad 67$$

$$F_{gas,O_2} = k \cdot ([O_2]_{sat} - [O_2]) \cdot (1 - A) \quad 68$$

469

470 where k is the gas transfer velocity, [CO<sub>2</sub>]<sub>sat</sub> and [O<sub>2</sub>]<sub>sat</sub> are saturation concentrations, and  
471 A is the fractional ice-covered area that is calculated by the physical model. Gas transfer  
472 velocity k is a function of wind speed (u) following Wanninkhof (1992) where Sc is the  
473 Schmidt Number for a specific gas:

474

$$k = 0.31 \cdot u^2 \cdot \left(\frac{Sc}{660}\right)^{-0.5}$$

475

476 **3 Results and Discussion**

477 All new results from MESMO 3 presented here are from the steady state. On a single  
 478 compute core at the Minnesota Supercomputing Institute, it takes approximately 1 hour to  
 479 complete 1,000 years of MESMO 3 simulation. The "standard" MESMO 3 has the power law  
 480 model of flexible stoichiometry but no DOM<sub>r</sub>. The results from the standard model  
 481 (hereafter just MESMO 3) are presented in Section 3.1, and the results from the DOM<sub>r</sub>-  
 482 enabled model are presented in Section 3.2. In Table 3, we summarize and compare key  
 483 biogeochemical diagnostics from MESMO 3 against those from MESMO 2 and available  
 484 observational constraints. The global NPP, as well as global export production of POC and  
 485 opal, are comparable or somewhat lower in MESMO 3 than MESMO 2.

486

487 We relied on experience to calibrate MESMO 3 with the primary goal of reasonably  
 488 simulating the phytoplankton community composition and C:N:P ratio (e.g., abundant  
 489 cyanobacteria and high ratio for all PFTs in oligotrophic gyres). We tried to improve or at  
 490 least preserve the gains that we achieved in earlier versions of MESMO in terms of the  
 491 global distributions of PO<sub>4</sub>, NO<sub>3</sub>, O<sub>2</sub>, Si(OH)<sub>4</sub>, and FeT (Supplemental Figures S1, S2, S3, S4,  
 492 and S5). Overall, there is a stronger nutrient depletion in the new model. For example, the  
 493 surface PO<sub>4</sub> and NO<sub>3</sub> in MESMO 3 are now sufficiently depleted in the subtropical gyres but  
 494 too low in the eastern equatorial Pacific when compared to the World Ocean Atlas (Figure  
 495 S1; see RMSE in Table 3). It is a challenge for MESMO and other coarse resolution models to  
 496 simulate narrow dynamical features such as equatorial upwelling and reproduce  
 497 biogeochemical features with sharp gradients. The spatial pattern of POC export that drives  
 498 this surface nutrient pattern is similar in the two models (Figure S2). In the 1D global  
 499 profile, there is a marked improvement in the subsurface distribution of O<sub>2</sub> in MESMO 3  
 500 over MESMO 2. Whereas the depth of the oxygen minimum was ~300 m in MEMOS 2, it is  
 501 ~1000 m in both MESMO 3 and the World Ocean Atlas (Figure S3). At 1000 m, the O<sub>2</sub>  
 502 minimum is located in the far North Pacific in MESMO 3, whereas in the World Ocean Atlas



503 it occurs in both the Northeast Pacific and the Arabian Sea. In contrast, the world ocean at  
504 1000 m is too well-oxygenated in MESMO 2. We believe that the improved match in the O<sub>2</sub>  
505 minimum depth would help simulate denitrification in the correct depth range, and there is  
506 a modest improvement in the data-model O<sub>2</sub> mismatch in terms of RMSE in MESMO 3 over  
507 MESMO 2 (Table 3). The deepening of the O<sub>2</sub> minimum was achieved largely by increasing  
508 the particle sinking speed, which tends to strengthen the biological pump and deplete the  
509 surface nutrients. This also helps MESMO 3 preserves MESMO 2's surface Si(OH)<sub>4</sub> depletion  
510 in much of the world ocean except in the North Pacific and Southern Ocean (Figure S4).  
511 This is a feature captured by Si\* < 0 (Si\* = [Si(OH)<sub>4</sub>] - [NO<sub>3</sub>]) in observations (Sarmiento et al.,  
512 2004) and simulated previously by MESMO 2 and now MESMO 3. Finally, surface FeT is also  
513 depleted more strongly in MESMO 3 over MESMO2, except the North Atlantic, where  
514 aeolian deposition of dust from the Sahara maintains a steady Fe supply (Figure S5).

515  
516 In MESMO 3, we made no effort to calibrate all the semi-labile pools of DOM: DOC<sub>sl</sub>, DOP<sub>sl</sub>,  
517 DON<sub>sl</sub>, and DOFe<sub>sl</sub>. We note only that the surface DOC<sub>sl</sub> concentration of 58 μmol kg<sup>-1</sup> and  
518 DOC export production of 1.4 Pg C yr<sup>-1</sup> in MESMO 3 are higher than in MESMO 2 (24 μmol  
519 kg<sup>-1</sup> and 0.4 Pg C yr<sup>-1</sup>, respectively). The higher surface concentration is due to the longer τ<sub>sl</sub>  
520 in MESMO 3 (Table 2d). The global average of the temperature dependent fDOM in MESMO  
521 3 is 0.69, which is slightly higher than the spatially uniform value of 0.67 in MESMO 2.

522

### 523 **3.1 Novel features of MESMO 3**

524 An important new feature of MESMO 3 is the representation of the primary producers by  
525 three PFTs (Figure 2). The eukaryotes are characterized by the highest maximum growth  
526 rate and high half-saturation constants. Thus, the eukaryotes are more dominant than the  
527 other PFTs in the more eutrophic waters of the equatorial and polar regions (Figure 2a).  
528 The cyanobacteria have smaller half-saturation constants and thus are more dominant in  
529 the oligotrophic subtropical gyres (Figure 2c). The diazotrophs do not have NO<sub>3</sub> limitation  
530 but have the lowest maximum growth rate. Thus it is much lower in abundance than the  
531 other two PFTs generally, and outcompeted in transient blooms and thus excluded in  
532 higher latitudes (Figure 2e).

533

534 Figure 2 also indicates that all three PFTs show Fe limitation in the Southern Ocean.  
535 Outside the Southern Ocean, the eukaryotes are primarily limited by  $\text{Si(OH)}_4$  (Figure 2b).  
536 As far as organic carbon is concerned, we consider the eukaryotes to basically represent  
537 diatoms, which are arguably the most important agent of organic carbon export. In this  
538 context, the widespread silica limitation for eukaryotes would be consistent with the  
539 notions that silica uptake by diatoms should be limited in  $\sim 60\%$  of the world surface ocean  
540 (Ragueneau et al. 2000) and that much the world ocean thermocline is filled with silica-  
541 depleted water ( $\text{Si}^* < 0$  as noted above). On the other hand, the cyanobacteria are largely  
542 limited by  $\text{NO}_3$  outside the Southern Ocean (Figure 2d). The diazotrophs are limited by iron  
543 in much of the world ocean except in the Atlantic basin (Figure 2f), where surface  $\text{PO}_4$  is  
544 strongly depleted in both observations (Mather et al., 2008) and in our model (Figure S1).

545

546 Figure 3 illustrates the influence of the RNPG index, which was implemented in MESMO 3  
547 to allow for the effect of competition between diatoms and coccolithophores within the  
548 same PFT (Equations 22 and 23). The eukaryote NPP (Figure 3a) is effectively split into two  
549 parts: one is associated with diatoms and opal production (Figure 3b), and the other is  
550 associated with coccolithophores and  $\text{CaCO}_3$  production (Figure 3c). According to the RNPG  
551 index, opal production is simulated more in the higher latitudes of the Southern Ocean and  
552 the North Pacific, where surface  $[\text{Si(OH)}_4]$  is abundant. Elsewhere,  $\text{CaCO}_3$  production is  
553 relatively larger. The decoupling is prominent in the North Indian. Note that the spatial  
554 pattern of  $\text{CaCO}_3$  production is quite different in MEMOS 3 (Figure 3c) and MESMO 2  
555 (Figure 3d), because  $\text{CaCO}_3$  production was associated in MESMO 2 with the "small" PFT,  
556 which corresponds to the cyanobacteria PFT in MESMO 3.

557

558 The global pattern of the mean C:P uptake ratio in the production layer is shown in Figure  
559 4. Consistent with observations (Martiny et al., 2013), the simulated C:P ratio of the  
560 phytoplankton community is elevated in the oligotrophic subtropical gyres and low in the  
561 eutrophic polar waters (Figure 4a). The community C:P ratio exceeds 200 in the gyres and  
562 reaches as low as 40-50 in the Southern Ocean. The community C:P has contributions from  
563 both physiological effects (i.e., environmental drivers acting on each PFT's C:P ratio) and

564 taxonomic effects (i.e., the shift in the community composition changes the weighting of  
565 each PFT's C:P ratio). Figure 4b shows that the community C:P is high in oligotrophic gyres  
566 because cyanobacteria and to a lesser extent diazotrophs dominate the community, and  
567 their C:P ratio is high. Conversely, the community C:P is low in the polar waters because the  
568 eukaryotes dominate and their C:P ratio is low. For both eukaryotes and cyanobacteria,  
569 their C:P is high in oligotrophic subtropical gyres because  $PO_4$  is low (Figure 4c and d). This  
570 physiological effect is larger in eukaryotes than cyanobacteria because the former has  
571 greater sensitivity (i.e., larger sensitivity factor  $s_{PO_4}^{P:C}$ , Equation 5, Table 2b). However, the  
572 cyanobacteria PFT's C:P ratio has an additional sensitivity to temperature (i.e.,  $s_T^{P:C} \neq 0$ )  
573 that elevates their C:P in the lower latitudes. We do not show the C:P ratio for diazotrophs  
574 because it is very similar to that of cyanobacteria (Figure 4b, d).

575

576 In order to gain more insights into the spatial patterns of the C:P ratio (Figure 4), we  
577 examined the relationships between the C:P and C:N ratios and the four possible  
578 environmental drivers for eukaryotes and cyanobacteria (Figure 5; again, diazotrophs are  
579 not shown). The red plots show that there is a causal relationship between the ratios and  
580 the drivers as formulated by the power law model (Equations 5 and 6). The black plots  
581 show the absence of a causal relationship. For example, the C:P ratio of both eukaryotes  
582 and cyanobacteria are strongly correlated with  $PO_4$  because there is a causal relationship  
583 (Figure 5a, b shown in red). Similarly, the C:N ratio of the same two PFTs have a strong  
584 correlation with  $PO_4$  (Figure 5c, d in black), but there is actually not a causal relationship  
585 (i.e.,  $s_{PO_4}^{N:C} = 0$ , Table 2b). The C:N- $PO_4$  correlation exists, simply because the nutrients are  
586 well correlated. Similarly, because temperature and photosynthetically active radiation  
587 (PAR) tend to be correlated via latitude, the stoichiometry has a similar correlation to the  
588 two drivers. For example, cyanobacteria C:P has a strong correlation with both  
589 temperature and PAR (Figure 5j, 4n), but only the temperature is a real driver. Figure 5  
590 indicates which are the dominant drivers of the C:N:P ratio in MESMO 3. For the eukaryote  
591 C:P ratio, it is  $PO_4$ . For the cyanobacteria C:P ratio, the important drivers are temperature  
592 and  $PO_4$ . For the C:N ratio for both eukaryotes and cyanobacteria,  $NO_3$  is more important  
593 than PAR. Figure 5 also serves to remind us that correlation does not indicate causation.

594

595 Figure 6 shows the community C:P and C:N ratios plotted against the four environmental  
596 drivers. Unlike Figure 5, which reflected the individual PFT's physiological response, Figure  
597 6 includes the effect of taxonomy as well. Still, the effects of  $\text{PO}_4$  and temperature are  
598 clearly visible on the community C:P ratio. Both low  $[\text{PO}_4]$  and warmer waters are found in  
599 the lower latitudes, so the P frugality and temperature effects are additive. The effect of  
600  $\text{NO}_3$  on the community C:N ratio is also very clear, but the effect of PAR is not as clear. Thus  
601 overall, the physiological effects seen in the PFT-specific C:N:P are obvious in the  
602 community C:N:P ratio.

603

### 604 **3.2 $\text{DOM}_r$ -enabled MESMO 3**

605 In MESMO 2,  $\text{DOC}_{\text{sl}}$  was a standard state variable. In MESMO 3, other forms of DOM are  
606 available as options. They are the semi-labile forms of DOM:  $\text{DOP}_{\text{sl}}$ ,  $\text{DON}_{\text{sl}}$ , and  $\text{DOFe}_{\text{sl}}$ ; and  
607 the refractory forms of DOM:  $\text{DOC}_r$ ,  $\text{DOP}_r$ , and  $\text{DON}_r$ . MESMO 3 is not yet calibrated with  
608 respect to all the DOM variables, but here we demonstrate their potential use in future  
609 biogeochemical investigations by presenting steady state DOM results from the model  
610 experiment *LV* (experiment ID: 210310m). In this run, all three sinks of  $\text{DOM}_r$  are activated:  
611 slow background decay, photodegradation, and degradation in hydrothermal vents.

612

613 The experiment name *LV* stands for "literature values." In *LV*, we use the literature values  
614 for the key DOM remineralization model parameters (Table 2d) and  $f\text{DOM}_r = 0.01$  (Hansell,  
615 2013). All other model parameter values in the *LV* run are identical to the standard MESMO  
616 3 model (Table 2). The black lines in Figure 7 show the global mean vertical profiles of the  
617 total DOC ( $\text{DOC}_t = \text{DOC}_{\text{sl}} + \text{DOC}_r$ ) in solid line and  $\text{DOC}_r$  in dashed line. Qualitatively, the  
618 simulated profiles are consistent with the observations, showing a near-uniform  $\text{DOC}_r$   
619 concentration and a  $\text{DOC}_{\text{sl}}$  profile that rapidly with depth in the top few hundred meters  
620 (Hansell, 2013). However, the simulated values reach  $130 \mu\text{mol kg}^{-1}$  in the surface, which is  
621 approximately twice the observations. More typically, the observed  $\text{DOC}_r$  is  $30\sim 40 \mu\text{mol kg}^{-1}$   
622  $^1$ , and the observed  $\text{DOC}_{\text{sl}}$  attenuates with depth from  $30\sim 40 \mu\text{mol kg}^{-1}$  near the surface. So

623 their sum, which is represented by  $\text{DOC}_t$ , is approximately  $60\text{-}80 \mu\text{mol kg}^{-1}$  at the surface in  
624 observations.

625

626 Figure 8 adds a lateral perspective to Figure 7. The rapid  $\text{DOC}_t$  attenuation in the vertical is  
627 strong in the lower latitudes where stratification is generally stronger. The transport of  
628  $\text{DOC}_{sl}$  from the surface to deeper waters is evident in the high latitudes of the North  
629 Atlantic and the Southern Ocean. The  $\text{DOC}_t$  change in the deep ocean is limited.

630 Observations of deep ocean  $\text{DOC}_t$  indicates a reduction by 29% or  $14 \mu\text{mol kg}^{-1}$  from the  
631 deep North Atlantic to the deep North Pacific (Hansell and Carlson, 1998). Figure 8 shows  
632 that the deep ocean  $\text{DOC}_t$  gradient in *LV* is approximately  $10 \mu\text{mol kg}^{-1}$  from  $70\text{-}75 \mu\text{mol kg}^{-1}$   
633  $^1$  in the North Atlantic to  $<65 \mu\text{mol kg}^{-1}$  in the North Pacific.

634

635 The horizontal  $\text{DOC}_t$  distributions from the *LV* run can also be compared to a global  
636 extrapolation based on an artificial neural network (ANN) of the available  $\text{DOC}_t$  data  
637 (Roshan and DeVries, 2017). At the surface, the extrapolation indicates higher  $\text{DOC}_t$   
638 concentrations in the subtropical gyres (Figure 9a), while our simulation does not clearly  
639 delineate the gyres (Figure 9c). In our model, *fDOM* is temperature-dependent and strongly  
640 controls the production of DOM. The surface  $\text{DOC}_t$  is thus more elevated in the lower  
641 latitudes. Interestingly, the ANN study diagnosed higher rates of DOM production in the  
642 subtropical gyres. Since the oligotrophic subtropical gyres have low NPP, the diagnosis  
643 would thus suggest that somehow *fDOM* is higher in the gyres. At depths, both the  
644 extrapolated and simulated  $\text{DOC}_t$  show a gradual decline in concentrations from the North  
645 Atlantic to the North Pacific (Figure 9b, d). The highest deep  $\text{DOC}_t$  in the *LV* run is seen just  
646 south of Greenland, where convection occurs in the model.

647

648 Finally, we show that the deep ocean radiocarbon aging is larger in DIC than in  $\text{DOC}_t$  in the  
649 model (Figure 10). The North Pacific-North Atlantic  $\Delta^{14}\text{C}$  gradient is roughly  $-100\text{‰}$  for  
650 DIC and  $-70\text{‰}$  for  $\text{DOC}_t$ . The oldest  $\text{DOC}_t$   $\Delta^{14}\text{C}$  is approximately  $-430\text{‰}$  in the North Pacific.  
651 If  $^{14}\text{C}$  decay were the only mechanism of change along the path of the deepwater  
652 circulation, the  $\Delta^{14}\text{C}$  gradient should be quite similar between DIC and  $\text{DOC}_t$ , which are both

653 dissolved phases and transported passively by the same circulation. The one potentially  
654 important difference is that the addition of the relatively young  $DI^{14}C$  and  $DO^{14}C$  to the  
655 deep ocean by the "deep POC split" (see Section 2.3) impacts  $DOC_t \Delta^{14}C$  more than  $DIC \Delta^{14}C$ ,  
656 because  $DOC_t$  is two orders of magnitude lower in concentration than  $DIC$ .

657  
658 In observations, the aging of  $DIC$  and  $DOC_t$  is reportedly similar in the Antarctic Bottom  
659 Water (below 4000 m) of the deep Pacific (Druffel et al., 2019). This may be explained by  
660 the fact that there would not be much deep POC split occurring so deep in the ocean. The  
661 North Pacific-North Atlantic  $\Delta^{14}C$  gradient, accounting for thermonuclear bomb  $^{14}C$ , may be  
662 as large as  $-100\text{‰}$  for  $DOC_t$  (about  $-550\text{‰}$  in the deep Pacific and  $-456\text{‰}$  in the deep  
663 Atlantic) (Druffel et al., 2019). This gradient is not rigorously determined, because there is  
664 not enough data to do an objective analysis. Therefore, the equivalent  $\Delta^{14}C$  gradient for  $DIC$   
665 cannot be determined. However, the  $DIC \Delta^{14}C$  endmember values by inspection (about -  
666  $250\text{‰}$  in the deep Pacific and  $-70\text{‰}$  in the deep Atlantic) (Matsumoto and Key, 2004)  
667 indicate a clearly larger  $\Delta^{14}C$  gradient for  $DIC$  than  $DOC_t$  as simulated by the experiment *LV*.

668  
669 One lesson from the data-*LV* run mismatch in the overall  $DOC_t$  concentration (Figure 7) and  
670 surface  $DOC_t$  pattern (Figure 9) is that the parameter values from the literature do not fully  
671 capture the DOC cycle and/or MESMO 3 is still lacking some important DOC process. In *LV*,  
672 the surface  $DOC_t$  is too high because  $DOC_r$  is too high, while  $DOC_{sl}$  is not unreasonable  
673 (Figure 7).  $DOC_r$  is too high because there is too much  $DOC_r$  production (e.g.,  $fDOM_r=1\%$  is  
674 too large), there is too little  $DOC_r$  degradation (e.g., one of the DOM decay mechanisms is  
675 too slow; Equation 28 and Table 2d), or some combination of both. For example,  $fDOM_r$  is a  
676 key parameter that is not well constrained by observations. Had we used  $0.2\%$  instead of  
677  $1\%$  for  $fDOM_r$ , the global mean surface  $DOC_t$  drops to  $76 \mu\text{mol kg}^{-1}$  (red line, Figure 7),  
678 consistent with observations. For achieving a better surface  $DOC_t$  pattern, we may need a  
679 different formulation of  $fDOM$  that is, for example, negatively related to nutrient  
680 concentrations so that  $fDOM$  increases in the oligotrophic subtropical gyres (Roshan and  
681 DeVries, 2017).

682

683 Another lesson from the DOM modeling exercise is that it is important to simulate  $\text{DOP}_r$   
684 reasonably well in order to preserve the favorable results we achieved in MESMO 3 with  
685 respect to biological production and the phytoplankton C:N:P ratio. We find that in the  
686 experiment *LV*, the global mean  $\text{DOP}_r$  concentration becomes steady at  $0.45 \mu\text{mol-P kg}^{-1}$ . In  
687 observations, the mean  $\text{DOC}_r$  is about  $40 \mu\text{mol-C kg}^{-1}$ , and the  $\text{DOC}_r:\text{DOP}_r$  ratio is estimated  
688 to be  $\sim 1370:1$  (Letscher and Moore, 2015), so  $\text{DOP}_r$  concentration should only be roughly  
689  $0.03 \mu\text{mol-P kg}^{-1}$ . Thus, the simulated  $\text{DOP}_r=0.45 \mu\text{mol-P kg}^{-1}$  is an order of magnitude too  
690 high. Because there is more P in the form of  $\text{DOP}_r$  in *LV*, the oceanic inventory of  $\text{PO}_4$   
691 declines, causing a nearly 10% drop in export production compared to the standard  
692 MESMO 3. In *LV*, the decline in the surface ocean  $\text{PO}_4$  that accompanies the change in the  
693  $\text{PO}_4$  inventory acts on the phytoplankton physiology (i.e., P effect on C:P in Equation 5),  
694 which leads to a large rise in the global mean phytoplankton community C:P export ratio  
695 from 113:1 to 127:1. The implementation of preferential remineralization of DOP (and  
696 DON) over DOC (Letscher and Moore, 2015) is one way to deal with the problem of too high  
697  $\text{DOP}_r$  concentrations.

698

### 699 **3.3 Large-scale patterns of $\text{N}_2$ fixation and denitrification**

700 The modeled habitat of diazotrophs is concentrated in tropical and subtropical waters  
701 between  $40^\circ\text{S}$  and  $40^\circ\text{N}$  and limited by iron (Figure 1e, f). Most noticeably in North Pacific  
702 subtropical gyre, diazotrophs constitute  $\sim 40\%$  of total NPP. The latitudinal extent of  
703 diazotrophs is mainly determined by surface nitrate availability and physical factors such  
704 as surface temperature and irradiance. Low nitrate availability in subtropical gyres gives  
705 diazotrophs a competitive advantage over small cyanobacteria. Warm temperature and  
706 high irradiance also critical physical factors that drive the growth of diazotrophs in the  
707 model.

708

709 The modeled global depth-integrated  $\text{N}_2$  fixation is  $101 \text{ Tg N yr}^{-1}$  (Table 3), and this value  
710 falls well within the range of observational and geochemical constraints of  $80 - 200 \text{ Tg N}$   
711  $\text{yr}^{-1}$  (Landolfi et al., 2018). In MESMO 3,  $\text{N}_2$  fixation occurs in the North Pacific and mid-to-  
712 low latitudes of the Atlantic basin (Supplementary Figure S6), where diazotrophs are

713 generally more abundant (Figure 2e). The elevated  $N_2$  fixation rate in the North Pacific,  
714 where nitrate limits eukaryotes and cyanobacteria (Figure 2b, d), can be explained by the  
715 healthy growth of diazotrophs, which is not limited by N. In the subtropical and tropical  
716 Atlantic and the Indian Ocean, high  $N_2$  fixation is driven by elevated C:P and N:P ratio  
717 (Figure 4), exemplified by low phosphate availability and warm surface temperature. This  
718 spatial pattern agrees with a recent inverse model study (Wang et al., 2019), which showed  
719 an elevated  $N_2$  fixation rate in subtropical gyres.

720

721 Global water-column denitrification is  $101 \text{ Tg N yr}^{-1}$  (Table 3) and is equal to the global  $N_2$   
722 fixation because the model has reached steady state. Denitrification is restricted to the  
723 subpolar North Pacific (Figure S6), where sub-surface oxygen concentration is significantly  
724 depleted (Figure S3d). Enhanced denitrification in this region is in qualitative agreement  
725 with a previous modeling study (Bianchi et al., 2018), which showed the anaerobic niche  
726 due to particle microenvironments can significantly expand the hypoxic expanses in the  
727 North Pacific. However, the extent of denitrification in our model does not include the  
728 eastern equatorial Pacific and northern Indian, which are important hotspots for  
729 denitrification (Codispoti, 2007; Deutsch et al., 2007). This issue is typical of coarse-  
730 resolution global ocean biogeochemistry models that lack spatial resolution in reproducing  
731 intense upwelling (Marchal et al., 1998; Najjar et al., 1992; Yamanaka and Tajika, 1997).

732

733 Finally, the ratio of the global inventories of  $NO_3$  and  $PO_4$  in MESMO 3 is just about 16 at  
734 steady state, consistent with observations (Gruber and Sarmiento, 1997). One key model  
735 parameter in this regard is the nitrate uptake half saturation constant of diazotrophs,  $K_{NO_3,3}$   
736 in Equation 2. A large value of  $K_{NO_3,3}$  will make it hard for diazotrophs to obtain fixed N  
737 from  $NO_3$ , which would facilitate  $N_2$  fixation and pushes up the global N/P ratio. With a  
738 smaller value of  $K_{NO_3,3}$ , diazotrophs will more easily uptake  $NO_3$ , thus depressing  $N_2$   
739 fixation, lowering the global N/P ratio.

740

#### 741 **4. Conclusions**

742 MESMO 3, the third and latest version of MESMO, is comprehensively described here. With  
743 a fully flexible C:N:P ratio in three PFTs, a prognostic N cycle, and more mechanistic



744 schemes of organic matter production and remineralization, MESMO 3 reflects the evolving  
745 and accumulating knowledge of the ocean biogeochemistry. The model thus remains an  
746 effective tool for investigations of the global biogeochemical cycles especially on long time  
747 scale given the model's computational efficiency. In particular, MESMO 3 holds promise for  
748 studying the marine DOM cycle. The optional features of MESMO 3 include the semi-labile  
749 and refractory pools of C, P, N, and Fe. The fact that the literature values regarding the  
750 present marine DOM cycle are unable to simulate key observations indicates an  
751 opportunity for MESMO 3 to contribute to an improved understanding of the marine DOM  
752 cycle.

753

#### 754 **Code availability**

755 The complete code of MESMO version 3.0 and results presented here are available at  
756 GitHub <https://github.com/gaia3intc/mesmo.git> and have a DOI:  
757 10.5281/zenodo.4403605.

758

#### 759 **Author contribution**

760 KM, TT, and JZ developed the model code. KM performed the simulations, carried out  
761 analyses, and archived the model code and results. KM and TT wrote the paper.

762

#### 763 **Acknowledgements**

764 This work was funded by the US National Science Foundation (OCE-1827948). Numerical  
765 modeling and analysis were carried out using resources at the University of Minnesota  
766 Supercomputing Institute.

767

768 **Tables**

769

770 **Table 1.** MESMO Development

771 PFT = phytoplankton functional types. MESMO2 PFTs are LG = large/diatoms and SM = small.  
772 MESMO 3 PFTs are Eu = eukaryotes, Cy = cyanobacteria, and Dz = diazotrophs. OM = organic  
773 matter. RNPG = residual nitrate potential growth. T = temperature. PAR = photosynthetically  
774 active radiation. fDOM = fraction of NPP routed to dissolved organic matter (DOM). The two  
775 types of DOM are semi-labile (DOC, DOP, DON, and DOFe) and refractory (DOCr, DOPr, and  
776 DONr). Carbon isotopes (<sup>12</sup>C, <sup>13</sup>C, and <sup>14</sup>C) are calculated separately for DOC and DOCr. The  
777 run ID is 210310m for the MESMO 3 experiment LVR and 210310o for the experiment LVR  
778 with fDOM<sub>r</sub>=0.2%.

779

780

781 **Table 2.** MESMO 3 Biogeochemical Model Parameters Values

782

783 **Table 3.** Key Biogeochemical Model Diagnostics

784 <sup>a</sup>NPP for MESMO 2 was unavailable as a model output and therefore estimated from POC  
785 and fDOM=0.67. <sup>b</sup>NPP (in terms of C) is needed in the calculation of the PFT abundance. The  
786 root mean square error (RMSE) of the simulated P, N, Si, and O<sub>2</sub> distributions from MESMO  
787 2 and 3 was calculated relative to the World Ocean Atlas 2018 gridded data (Garcia et al.,  
788 2018, 2019). The model-data comparison is made in the top 100 m for nutrients and below  
789 100 m for O<sub>2</sub>. WOA18 was regridded to the MESMO 3 grid to calculate the RMSE.

790

791

792 References for independent constraints: (1) global NPP (Carr et al., 2006); (2) global POC  
793 export (DeVries and Weber, 2017); (3) global DOC export assumed to be 20% of total  
794 carbon export (Hansell et al., 2009; Roshan and DeVries, 2017); (4) global opal (Dunne et  
795 al., 2007); (5) global CaCO<sub>3</sub> export (Berelson et al., 2007); (6) global N fixation and  
796 denitrification rates (Landolfi et al., 2018); (7) uptake C:N:P ratio is based on POM  
797 measurements (Martiny et al., 2013); (8) export C:N:P ratio is assumed to equal the  
798 subsurface remineralization ratio (Anderson and Sarmiento, 1994); (9) Deep O<sub>2</sub> from  
799 WOA18 below 100 m (Garcia et al., 2019).

800

801

802

803

804 **Figures**

805

806 **Figure 1.** Schematic diagram of DOM cycling in MESMO 2 versus MESMO 3. In the new  
807 model,  $DOM_r$  can be activated.  $DOM_r$  is produced from POM breakdown, which can occur in  
808 the production layer or throughout the water column in the "deep POC split." Possible  
809  $DOM_r$  remineralization mechanisms are the slow background degradation that occurs  
810 everywhere, thermal degradation in hydrothermal vents, and photodegradation in the  
811 surface. See text for details.

812

813 **Figure 2.** NPP-based surface phytoplankton functional type (PFT) abundance and nutrient  
814 limitation in MESMO 3. Fractional abundance and nutrient limitation for eukaryotes (a, b),  
815 cyanobacteria (c, d), and diazotrophs (e, f).

816

817 **Figure 3.** Eukaryote production in MESMO 3 and  $CaCO_3$  export in MESMO 2. In MESMO 3,  
818 eukaryote NPP (a) is linked to both opal export (b) and  $CaCO_3$  export (c) but the two export  
819 productions are differentiated by the residual nitrate potential growth (RNPG). Compare  
820  $CaCO_3$  export in MESMO 3 (c) to MESMO 2 (d). Unit =  $\text{mol m}^{-2} \text{ year}^{-1}$ .

821

822 **Figure 4.** Uptake C:P ratio in the top 100 m in MESMO 3: (a) phytoplankton community C:P,  
823 (b) zonal mean C:P of all three PFTs and phytoplankton community, (c) eukaryote C:P, and  
824 (d) cyanobacteria C:P. The colors in (b) indicate: black = community C:P, red = eukaryote  
825 C:P, green = cyanobacteria C:P, and blue = diazotroph C:P. Also, (b) shows the range of  
826 observed C:P ratio binned by latitude (Martiny et al., 2013).

827

828 **Figure 5.** Scatter plots of surface ocean eukaryote and cyanobacteria C:P and C:N vs.  
829 environmental drivers in MESMO 3. Columns: 1 = eukaryote C:P, 2 = cyanobacteria C:P, 3 =  
830 eukaryote C:N, and 4 = cyanobacteria C:N. Rows: 1 =  $PO_4$ , 2 =  $NO_3$ , 3 = temperature, and 4 =  
831 PAR. Red indicates causal relationship according to the power law formulation of flexible  
832 C:N:P ratio. PAR = photosynthetically active radiation in  $W m^{-2}$ .

833

834 **Figure 6.** Scatter plots of surface ocean community C:P and C:N vs environmental drivers in  
835 MESMO 3.

836

837 **Figure 7.** Global mean vertical profiles of DOC from the DOM<sub>R</sub>-enabled MESMO 3. DOC<sub>t</sub>  
838 (DOC<sub>SI</sub>+DOC<sub>R</sub>, black line) and DOC<sub>R</sub> (black dashed line) from the *LV* run. Red line is DOC<sub>t</sub>  
839 after reducing fDOM<sub>r</sub> from 1% in *LV* to 0.2% (Experiment 210310o). Unit = μmol kg<sup>-1</sup>.

840

841 **Figure 8.** Global depth-latitude transect of DOC<sub>t</sub> from the DOM<sub>R</sub>-enabled MESMO 3 *LV* run.  
842 Transects are N-S along 25°W in the Atlantic, E-W along 60°S in the Southern Ocean, and N-  
843 S along 165°E in the Pacific. Unit = μmol kg<sup>-1</sup>.

844

845 **Figure 9.** Assessment of surface and deep ocean DOC<sub>t</sub> from the DOM<sub>R</sub>-enabled MESMO 3 *LV*  
846 run. Data-derived DOC<sub>t</sub> distributions in the top 100 m (a) and 2500-4000 m (b). Model-  
847 simulated DOC<sub>t</sub> distributions in the top 100 m (c) and 2500-4000 m (d). Date-derived DOC<sub>t</sub>  
848 are from Roshan and DeVries (Roshan and DeVries, 2017). Unit = μmol kg<sup>-1</sup>.

849

850 **Figure 10.** Δ<sup>14</sup>C of deep ocean DIC (a) and DOC<sub>t</sub> (b) from the DOM<sub>R</sub>-enabled MESMO 3 *LV*  
851 run. Vertical average over 2500-4000 m water depth. Unit = ‰.

852

853 **References:**

- 854 Anderson, L. A. and Sarmiento, J. L.: Redfield ratios of remineralization determined by  
855 nutrient data analysis, *Global Biogeochem. Cycles*, 8(1), 65–80,  
856 doi:10.1029/93GB03318, 1994.
- 857 Archer, D., Eby, M., Brovkin, V., Ridgwell, A., Cao, L., Mikolajewicz, U., Caldeira, K.,  
858 Matsumoto, K., Munhoven, G., Montenegro, A. and Tokos, K.: Atmospheric Lifetime of  
859 Fossil Fuel Carbon Dioxide, *Annu. Rev. Earth Planet. Sci.*, 37(1), 117–134,  
860 doi:10.1146/annurev.earth.031208.100206, 2009.
- 861 Arteaga, L., Pahlow, M. and Oschlies, A.: Global patterns of phytoplankton nutrient and light  
862 colimitation inferred from an optimality-based model, *Global Biogeochem. Cycles*,  
863 28(7), 648–661, doi:10.1002/2013GB004668, 2014.
- 864 Balch, W. M., Bates, N. R., Lam, P. J., Twining, B. S., Rosengard, S. Z., Bowler, B. C., Drapeau, D.  
865 T., Garley, R., Lubelczyk, L. C., Mitchell, C. and Rauschenberg, S.: Factors regulating the  
866 Great Calcite Belt in the Southern Ocean and its biogeochemical significance, *Global*  
867 *Biogeochem. Cycles*, 30(8), 1124–1144, doi:10.1002/2016GB005414, 2016.
- 868 Berelson, W. M., Balch, W. M., Najjar, R., Feely, R. A., Sabine, C. and Lee, K.: Relating  
869 estimates of CaCO<sub>3</sub> production, export, and dissolution in the water column to  
870 measurements of CaCO<sub>3</sub> rain into sediment traps and dissolution on the sea floor: A  
871 revised global carbonate budget, *Global Biogeochem. Cycles*, 21(1), 1–15,  
872 doi:10.1029/2006GB002803, 2007.
- 873 Bianchi, D., Weber, T. S., Kiko, R. and Deutsch, C.: Global niche of marine anaerobic  
874 metabolisms expanded by particle microenvironments, *Nat. Geosci.*, 11(4), 263–268,  
875 doi:10.1038/s41561-018-0081-0, 2018.
- 876 Brzezinski, M. A.: A switch from Si(OH)<sub>4</sub> to NO<sub>3</sub> – depletion in the glacial Southern Ocean,  
877 *Geophys. Res. Lett.*, 29(12), doi:10.1029/2001gl014349, 2002.
- 878 Cao, L., Eby, M., Ridgwell, A., Caldeira, K., Archer, D., Ishida, A., Joos, F., Matsumoto, K.,  
879 Mikolajewicz, U., Mouchet, A., Orr, J. C., Plattner, G.-K., Schlitzer, R., Tokos, K.,  
880 Totterdell, I., Tschumi, T., Yamanaka, Y. and Yool, A.: The role of ocean transport in the  
881 uptake of anthropogenic CO<sub>2</sub>, *Biogeosciences*, 6(3), 375–390, doi:10.5194/bg-6-375-  
882 2009, 2009.
- 883 Carr, M. E., Friedrichs, M. A. M., Schmeltz, M., Noguchi Aita, M., Antoine, D., Arrigo, K. R.,

884 Asanuma, I., Aumont, O., Barber, R., Behrenfeld, M., Bidigare, R., Buitenhuis, E. T.,  
885 Campbell, J., Ciotti, A., Dierssen, H., Dowell, M., Dunne, J., Esaias, W., Gentili, B., Gregg,  
886 W., Groom, S., Hoepffner, N., Ishizaka, J., Kameda, T., Le Quéré, C., Lohrenz, S., Marra, J.,  
887 Mélin, F., Moore, K., Morel, A., Reddy, T. E., Ryan, J., Scardi, M., Smyth, T., Turpie, K.,  
888 Tilstone, G., Waters, K. and Yamanaka, Y.: A comparison of global estimates of marine  
889 primary production from ocean color, *Deep. Res. Part II Top. Stud. Oceanogr.*, 53(5-7),  
890 741–770, doi:10.1016/j.dsr2.2006.01.028, 2006.

891 Cheng, H., Edwards, R. L., Southon, J., Matsumoto, K., Feinberg, J. M., Sinha, A., Zhou, W., Li,  
892 H., Li, X., Xu, Y., Chen, S., Tan, M., Wang, Q., Wang, Y., Ning, Y., Lawrence Edwards, R.,  
893 Southon, J., Matsumoto, K., Feinberg, J. M., Sinha, A., Zhou, W., Li, H., Li, X., Xu, Y., Chen,  
894 S., Tan, M., Wang, Q., Wang, Y. and Ning, Y.: Atmospheric  $^{14}\text{C}/^{12}\text{C}$  changes during the  
895 last glacial period from hulu cave, *Science* (80-. ), 362(6420), 1293–1297,  
896 doi:10.1126/science.aau0747, 2018.

897 Chien, C. Te, Pahlow, M., Schartau, M. and Oschlies, A.: Optimality-based non-Redfield  
898 plankton-ecosystem model (OPEM v1.1) in UVic-ESCM 2.9 - Part 2: Sensitivity analysis  
899 and model calibration, *Geosci. Model Dev.*, 13(10), 4691–4712, doi:10.5194/gmd-13-  
900 4691-2020, 2020.

901 Claussen, M., Mysak, L., Weaver, A., Crucifix, M., Fichefet, T., Loutre, M. F., Weber, S., Alcamo,  
902 J., Alexeev, V., Berger, A., Calov, R., Ganopolski, A., Goosse, H., Lohmann, G., Lunkeit, F.,  
903 Mokhov, I., Petoukhov, V., Stone, P. and Wang, Z.: Earth system models of intermediate  
904 complexity: Closing the gap in the spectrum of climate system models, *Clim. Dyn.*,  
905 18(7), 579–586, doi:10.1007/s00382-001-0200-1, 2002.

906 Codispoti, L. A.: An oceanic fixed nitrogen sink exceeding 400 Tg N a<sup>-1</sup> vs the concept of  
907 homeostasis in the fixed-nitrogen inventory, *Biogeosciences*, 4(2), 233–253,  
908 doi:10.5194/bg-4-233-2007, 2007.

909 Deutsch, C., Sarmiento, J. L., Sigman, D. M., Gruber, N. and Dunne, J. P.: Spatial coupling of  
910 nitrogen inputs and losses in the ocean, *Nature*, 445(7124), 163–167,  
911 doi:10.1038/nature05392, 2007.

912 DeVries, T. and Weber, T.: The export and fate of organic matter in the ocean: New  
913 constraints from combining satellite and oceanographic tracer observations, *Global*  
914 *Biogeochem. Cycles*, 31(3), 535–555, doi:10.1002/2016GB005551, 2017.

915 Druffel, E. R. M., Williams, P. M., Bauer, J. E. and Ertel, J. R.: Cycling of dissolved and  
916 particulate organic matter in the open ocean, *J. Geophys. Res.*, 97(C10), 15639,  
917 doi:10.1029/92JC01511, 1992.

918 Druffel, E. R. M., Griffin, S., Wang, N., Garcia, N. G., McNichol, A. P., Key, R. M. and Walker, B.  
919 D.: Dissolved Organic Radiocarbon in the Central Pacific Ocean, *Geophys. Res. Lett.*,  
920 46(10), 5396–5403, doi:10.1029/2019GL083149, 2019.

921 Dunne, J. P., Armstrong, R. A., Gnanadesikan, A. and Sarmiento, J. L.: Empirical and  
922 mechanistic models for the particle export ratio, *Global Biogeochem. Cycles*, 19(4),  
923 n/a-n/a, doi:10.1029/2004GB002390, 2005.

924 Dunne, J. P., Sarmiento, J. L. and Gnanadesikan, A.: A synthesis of global particle export from  
925 the surface ocean and cycling through the ocean interior and on the seafloor, *Global*  
926 *Biogeochem. Cycles*, 21(4), 1–16, doi:10.1029/2006GB002907, 2007.

927 Eby, M., Weaver, A. J., Alexander, K., Zickfeld, K., Abe-Ouchi, A., Cimadoribus, A. A., Crespin,  
928 E., Drijfhout, S. S., Edwards, N. R., Eliseev, A. V., Feulner, G., Fichefet, T., Forest, C. E.,  
929 Goosse, H., Holden, P. B., Joos, F., Kawamiya, M., Kicklighter, D., Kienert, H., Matsumoto,  
930 K., Mokhov, I. I., Monier, E., Olsen, S. M., Pedersen, J. O. P., Perrette, M., Philippon-  
931 Berthier, G., Ridgwell, A., Schlosser, A., Schneider von Deimling, T., Shaffer, G., Smith, R.  
932 S., Spahni, R., Sokolov, A. P., Steinacher, M., Tachiiri, K., Tokos, K., Yoshimori, M., Zeng,  
933 N. and Zhao, F.: Historical and idealized climate model experiments: an  
934 intercomparison of Earth system models of intermediate complexity, *Clim. Past*, 9(3),  
935 1111–1140, doi:10.5194/cp-9-1111-2013, 2013.

936 Edwards, N. R. and Marsh, R.: Uncertainties due to transport-parameter sensitivity in an  
937 efficient 3-D ocean-climate model, *Clim. Dyn.*, 24(4), 415–433, doi:10.1007/s00382-  
938 004-0508-8, 2005.

939 Eppley, R. W.: Temperature and phytoplankton growth in the sea, *Fish. Bull.*, 70(4), 1063–  
940 85, 1972.

941 Galbraith, E. D. and Martiny, A. C.: A simple nutrient-dependence mechanism for predicting  
942 the stoichiometry of marine ecosystems, *Proc. Natl. Acad. Sci.*, 112(27), 8199–8204,  
943 doi:10.1073/pnas.1423917112, 2015.

944 Garcia, H., Weathers, K. W., Paver, C. R., Smolyar, I., Boyer, T. P., Locarnini, R. A., Zweng, M.  
945 M., Mishonov, A. V., Baranova, O. K., Seidov, D. and Reagan, J. R.: *World Ocean Atlas*

946 2018. Volume 4: Dissolved Inorganic Nutrients (phosphate, nitrate and nitrate+nitrite,  
947 silicate), NOAA Atlas NESDIS 84, 84(July), 35, 2018.

948 Garcia, H. E., Weathers, K., Paver, C. R., Smolyar, I., Boyer, T. P., Locarnini, R. A., Zweng, M.  
949 M., Mishonov, A. V., Baranova, O. K., Seidov, D. and Reagan, J. R.: World Ocean Atlas  
950 2018, Volume 3: Dissolved Oxygen, Apparent Oxygen Utilization, and Oxygen  
951 Saturation, NOAA Atlas NESDIS, 3(83), 38 pp., 2019.

952 Gruber, N. and Sarmiento, J. L.: Global patterns of marine nitrogen fixation and  
953 denitrification, *Global Biogeochem. Cycles*, 11(2), 235–266, doi:10.1029/97GB00077,  
954 1997.

955 Hansell, D. A.: Recalcitrant Dissolved Organic Carbon Fractions, *Ann. Rev. Mar. Sci.*, 5, 421–  
956 445, doi:10.1146/annurev-marine-120710-100757, 2013.

957 Hansell, D. A. and Carlson, C. A.: Deep-ocean gradients in the concentration of dissolved  
958 organic carbon, *Nature*, 395(6699), 263–266, doi:10.1038/26200, 1998.

959 Hansell, D. A., Carlson, C. A., Repeta, D. J. and Schlitzer, R.: Dissolved Organic Matter in the  
960 Ocean: A Controversy stimulates new insights, *Oceanography*, 22(4), 202–211,  
961 doi:https://doi.org/10.5670/oceanog.2009.109, 2009.

962 Henson, S. A., Sanders, R., Madsen, E., Morris, P. J., Le Moigne, F. and Quartly, G. D.: A  
963 reduced estimate of the strength of the ocean’s biological carbon pump, *Geophys. Res.*  
964 *Let.*, 38(4), n/a-n/a, doi:10.1029/2011GL046735, 2011.

965 Hutchins, D. A. and Bruland, K. W.: Iron-limited growth and Si:N ratios in a costal upwelling  
966 regime, *Nature*, 393(June), 561–564, 1998.

967 Joos, F., Roth, R., Fuglestedt, J. S., Peters, G. P., Enting, I. G., Von Bloh, W., Brovkin, V., Burke,  
968 E. J., Eby, M., Edwards, N. R., Friedrich, T., Frölicher, T. L., Halloran, P. R., Holden, P. B.,  
969 Jones, C., Kleinen, T., Mackenzie, F. T., Matsumoto, K., Meinshausen, M., Plattner, G. K.,  
970 Reisinger, A., Segschneider, J., Shaffer, G., Steinacher, M., Strassmann, K., Tanaka, K.,  
971 Timmermann, A. and Weaver, A. J.: Carbon dioxide and climate impulse response  
972 functions for the computation of greenhouse gas metrics: A multi-model analysis,  
973 *Atmos. Chem. Phys.*, 13(5), 2793–2825, doi:10.5194/acp-13-2793-2013, 2013.

974 Kwiatkowski, L., Aumont, O., Bopp, L. and Ciais, P.: The Impact of Variable Phytoplankton  
975 Stoichiometry on Projections of Primary Production, Food Quality, and Carbon Uptake  
976 in the Global Ocean, *Global Biogeochem. Cycles*, 516–528,



977 doi:10.1002/2017GB005799, 2018.

978 Kwiatkowski, L., Aumont, O. and Bopp, L.: Consistent trophic amplification of marine  
979 biomass declines under climate change, *Glob. Chang. Biol.*, 25(1), 218–229,  
980 doi:10.1111/gcb.14468, 2019.

981 Landolfi, A., Kähler, P., Koeve, W. and Oschlies, A.: Global marine N<sub>2</sub> fixation estimates:  
982 From observations to models, *Front. Microbiol.*, 9(SEP), 1–8,  
983 doi:10.3389/fmicb.2018.02112, 2018.

984 Lang, S. Q., Butterfield, D. A., Lilley, M. D., Paul Johnson, H. and Hedges, J. I.: Dissolved  
985 organic carbon in ridge-axis and ridge-flank hydrothermal systems, *Geochim.  
986 Cosmochim. Acta*, 70(15), 3830–3842, doi:10.1016/j.gca.2006.04.031, 2006.

987 Laufkötter, C., John, J. G., Stock, C. A. and Dunne, J. P.: Temperature and oxygen dependence  
988 of the remineralization of organic matter, *Global Biogeochem. Cycles*, 31(7), 1038–  
989 1050, doi:10.1002/2017GB005643, 2017.

990 Laws, E. A., Falkowski, P. G., Smith, W. O., Ducklow, H. W. and McCarthy, J. J.: Temperature  
991 effects on export production in the open ocean, *Global Biogeochem. Cycles*, 14(4),  
992 1231–1246, doi:10.1029/1999GB001229, 2000.

993 Lee, S. Y., Chiang, J. C. H., Matsumoto, K. and Tokos, K. S.: Southern Ocean wind response to  
994 North Atlantic cooling and the rise in atmospheric CO<sub>2</sub>: Modeling perspective and  
995 paleoceanographic implications, *Paleoceanography*, 26, 1–16,  
996 doi:10.1029/2010PA002004, 2011.

997 Lenton, T. M., Williamson, M. S., Edwards, N. R., Marsh, R., Price, A. R., Ridgwell, A. J.,  
998 Shepherd, J. G. and Cox, S. J.: Millennial timescale carbon cycle and climate change in an  
999 efficient Earth system model, *Clim. Dyn.*, 26(7–8), 687–711, doi:10.1007/s00382-006-  
1000 0109-9, 2006.

1001 Letscher, R. T. and Moore, J. K.: Preferential remineralization of dissolved organic  
1002 phosphorus and non-Redfield DOM dynamics in the global ocean: Impacts on marine  
1003 productivity, nitrogen fixation, and carbon export, *Global Biogeochem. Cycles*, 29(3),  
1004 325–340, doi:10.1002/2014GB004904, 2015.

1005 Levitus, S.: Climatological atlas of the world ocean, US Department of Commerce, National  
1006 Oceanic and Atmospheric Administration., 1982.

1007 Mahowald, N. M., Muhs, D. R., Levis, S., Rasch, P. J., Yoshioka, M., Zender, C. S. and Luo, C.:

1008 Change in atmospheric mineral aerosols in response to climate: Last glacial period,  
1009 preindustrial, modern, and doubled carbon dioxide climates, *J. Geophys. Res. Atmos.*,  
1010 111(D10), n/a-n/a, doi:10.1029/2005JD006653, 2006.

1011 Marchal, O., Stocker, T. F. and Joos, F.: A latitude-depth, circulation-biogeochemical ocean  
1012 model for palaeoclimate studies. Development and sensitivities, *Tellus, Ser. B Chem.*  
1013 *Phys. Meteorol.*, 50B(3), 290–316, doi:10.1034/j.1600-0889.1998.t01-2-00006.x,  
1014 1998.

1015 Martiny, A. C., Pham, C. T. A. A., Primeau, F. W., Vrugt, J. A., Moore, J. K., Levin, S. A. and  
1016 Lomas, M. W.: Strong latitudinal patterns in the elemental ratios of marine plankton  
1017 and organic matter, *Nat. Geosci.*, 6(4), 279–283, doi:10.1038/ngeo1757, 2013.

1018 Mather, R. L., Reynolds, S. E., Wolff, G. A., Williams, R. G., Torres-Valdes, S., Woodward, E. M.  
1019 S., Landolfi, A., Pan, X., Sanders, R. and Achterberg, E. P.: Phosphorus cycling in the  
1020 North and South Atlantic Ocean subtropical gyres, *Nat. Geosci.*, 1(7), 439–443,  
1021 doi:10.1038/ngeo232, 2008.

1022 Matsumoto, K. and Key, R. M.: Natural radiocarbon distribution in the deep ocean, in *Global*  
1023 *Environmental Change in the Ocean and on Land*, edited by M. Shiyomi, H. Kawahata,  
1024 H. Koizumi, A. Tsuda, and Y. Awaya, pp. 45–58, Terrapub, Tokyo. [online] Available  
1025 from: <http://svr4.terrapub.co.jp/e-library/kawahata/pdf/045.pdf>, 2004.

1026 Matsumoto, K. and McNeil, B.: Decoupled response of ocean acidification to variations in  
1027 climate sensitivity, *J. Clim.*, 26, 1764–1771, doi:10.1175/JCLI-D-12-00290.1, 2012.

1028 Matsumoto, K. and Tanioka, T.: Shifts in regional production as a driver of future global  
1029 ocean production stoichiometry, *Environ. Res. Lett.*, 15(124027), doi:10.1088/1748-  
1030 9326/abc4b0, 2020.

1031 Matsumoto, K. and Yokoyama, Y.: Atmospheric  $\Delta 14\text{C}$  reduction in simulations of Atlantic  
1032 overturning circulation shutdown, *Global Biogeochem. Cycles*, 27(2), 296–304,  
1033 doi:10.1002/gbc.20035, 2013.

1034 Matsumoto, K., Tokos, K. S., Price, A. R. and Cox, S. J.: First description of the Minnesota  
1035 Earth System Model for Ocean biogeochemistry (MESMO 1.0), *Geosci. Model Dev.*, 1(1),  
1036 1–15, doi:10.5194/gmd-1-1-2008, 2008.

1037 Matsumoto, K., Tokos, K., Chikamoto, M. and Ridgwell, A.: Characterizing post-industrial  
1038 changes in the ocean carbon cycle in an Earth system model, *Tellus B Chem. Phys.*

1039 Meteorol., 62(4), 296–313, doi:10.1111/j.1600-0889.2010.00461.x, 2010.

1040 Matsumoto, K., Tokos, K., Huston, A. and Joy-Warren, H.: MESMO 2: a mechanistic marine  
1041 silica cycle and coupling to a simple terrestrial scheme, *Geosci. Model Dev.*, 6(2), 477–  
1042 494, doi:10.5194/gmd-6-477-2013, 2013.

1043 Matsumoto, K., Rickaby, R. and Tanioka, T.: Carbon Export Buffering and CO<sub>2</sub> Drawdown by  
1044 Flexible Phytoplankton C:N:P Under Glacial Conditions, *Paleoceanogr.  
1045 Paleoclimatology*, 35(7), 1–22, doi:10.1029/2019PA003823, 2020.

1046 Moore, J. K., Doney, S. C. and Lindsay, K.: Upper ocean ecosystem dynamics and iron cycling  
1047 in a global three-dimensional model, *Global Biogeochem. Cycles*, 18(4), 1–21,  
1048 doi:10.1029/2004GB002220, 2004.

1049 Mopper, K., Zhou, X., Kieber, R. J., Kieber, D. J., Sikorski, R. J. and Jones, R. D.: Photochemical  
1050 degradation of dissolved organic carbon and its impact on the oceanic carbon cycle,  
1051 *Nature*, 353(6339), 60–62, doi:10.1038/353060a0, 1991.

1052 Najjar, R. G., Sarmiento, J. L. and Toggweiler, J. R.: Downward transport and fate of organic  
1053 matter in the ocean: Simulations with a general circulation model, *Global Biogeochem.  
1054 Cycles*, 6(1), 45–76, doi:10.1029/91GB02718, 1992.

1055 Pahlow, M. and Oschlies, A.: Chain model of phytoplankton P, N and light colimitation, *Mar.  
1056 Ecol. Prog. Ser.*, 376(2), 69–83, doi:10.3354/meps07748, 2009.

1057 Pahlow, M. and Oschlies, A.: Optimal allocation backs droop’s cell-quota model, *Mar. Ecol.  
1058 Prog. Ser.*, 473(2010), 1–5, doi:10.3354/meps10181, 2013.

1059 Pahlow, M., Dietze, H. and Oschlies, A.: Optimality-based model of phytoplankton growth  
1060 and diazotrophy, *Mar. Ecol. Prog. Ser.*, 489, 1–16, doi:10.3354/meps10449, 2013.

1061 Pahlow, M., Chien, C. Te, Arteaga, L. A. and Oschlies, A.: Optimality-based non-Redfield  
1062 plankton-ecosystem model (OPEM v1.1) in UVic-ESCM 2.9 - Part 1: Implementation  
1063 and model behaviour, *Geosci. Model Dev.*, 13(10), 4663–4690, doi:10.5194/gmd-13-  
1064 4663-2020, 2020.

1065 Paulsen, H., Ilyina, T., Six, K. D. and Stemmler, I.: Incorporating a prognostic representation  
1066 of marine nitrogen fixers into the global ocean biogeochemical model HAMOCC, *J. Adv.  
1067 Model. Earth Syst.*, 9(1), 438–464, doi:10.1002/2016MS000737, 2017.

1068 Ridgwell, A.: Glacial-interglacial perturbations in the global carbon cycle, Ph. D. thesis, 134  
1069 pp., Univ. East Anglia, Norwich, U. K. Ridgwell, A. J., U. Edwards, 2001.

1070 Ridgwell, A., Hargreaves, J. C., Edwards, N. R., Annan, J. D., Lenton, T. M., Marsh, R., Yool, A.  
1071 and Watson, A.: Marine geochemical data assimilation in an efficient Earth System  
1072 Model of global biogeochemical cycling, *Biogeosciences*, 4(4), 87–104, doi:10.5194/bg-  
1073 4-87-2007, 2007.

1074 Ridgwell, A. J., Watson, A. J. and Archer, D. E.: Modeling the response of the oceanic Si  
1075 inventory to perturbation, and consequences for atmospheric CO<sub>2</sub>, *Global*  
1076 *Biogeochem. Cycles*, 16(4), 19-1-19–25, doi:10.1029/2002GB001877, 2002.

1077 Roshan, S. and DeVries, T.: Efficient dissolved organic carbon production and export in the  
1078 oligotrophic ocean, *Nat. Commun.*, 8(1), 2036, doi:10.1038/s41467-017-02227-3,  
1079 2017.

1080 Sarmiento, J. L., Gruber, N., Brzezinski, M. A. and Dunne, J. P.: High-latitude controls of  
1081 thermocline nutrients and low latitude biological productivity, *Nature*, 427(6969), 56–  
1082 60, doi:10.1038/nature02127, 2004.

1083 Sun, X. and Matsumoto, K.: Effects of sea ice on atmospheric p CO<sub>2</sub> : A revised view and  
1084 implications for glacial and future climates, *J. Geophys. Res.*, 115(G02015),  
1085 doi:10.1029/2009JG001023, 2010.

1086 Sunda, W. G. and Huntsman, S. A.: Iron uptake and growth limitation in oceanic and coastal  
1087 phytoplankton, *Mar. Chem.*, 50(1–4), 189–206, doi:10.1016/0304-4203(95)00035-P,  
1088 1995.

1089 Sverdrup, H. U.: On the conditions for the vernal blooming of phytoplankton, *J. Cons. Perm.*  
1090 *Int. Pour l'Exploration La Mer*, 18, 287–195, 1953.

1091 Takeda, S.: Influence of iron availability on nutrient consumption ratio, *Nature*, 393(JUNE),  
1092 774–777, 1998.

1093 Tanioka, T. and Matsumoto, K.: Buffering of Ocean Export Production by Flexible Elemental  
1094 Stoichiometry of Particulate Organic Matter, *Global Biogeochem. Cycles*, 31(10), 1528–  
1095 1542, doi:10.1002/2017GB005670, 2017.

1096 Tanioka, T. and Matsumoto, K.: A meta-analysis on environmental drivers of marine  
1097 phytoplankton C : N : P, *Biogeosciences*, 17(11), 2939–2954, doi:10.5194/bg-17-2939-  
1098 2020, 2020a.

1099 Tanioka, T. and Matsumoto, K.: Stability of Marine Organic Matter Respiration  
1100 Stoichiometry, *Geophys. Res. Lett.*, 47(1), 1–10, doi:10.1029/2019GL085564, 2020b.

1101 Ushie, H. and Matsumoto, K.: The role of shelf nutrients on glacial-interglacial CO<sub>2</sub>: A  
1102 negative feedback, *Global Biogeochem. Cycles*, 26, 1–10, doi:10.1029/2011GB004147,  
1103 2012.

1104 Wang, W.-L., Moore, J. K., Martiny, A. C. and Primeau, F. W.: Convergent estimates of marine  
1105 nitrogen fixation, *Nature*, 566(7743), 205–211, doi:10.1038/s41586-019-0911-2,  
1106 2019.

1107 Wanninkhof, R.: Relationship between wind speed and gas exchange over the ocean, *J.*  
1108 *Geophys. Res.*, 97(C5), 7373–7382, doi:10.1029/92JC00188, 1992.

1109 Weaver, A. J., Sedlá, J., Eby, M., Alexander, K., Crespin, E., Fichefet, T., Philippon-berthier, G.,  
1110 Joos, F., Kawamiya, M., Matsumoto, K., Steinacher, M., Tachiiri, K., Tokos, K., Yoshimori,  
1111 M. and Zickfeld, K.: Stability of the Atlantic meridional overturning circulation : A  
1112 model intercomparison, *Geophys. Res. Lett.*, 39, 1–7, doi:10.1029/2012GL053763,  
1113 2012.

1114 Yamanaka, Y. and Tajika, E.: Role of dissolved organic matter in the marine biogeochemical  
1115 cycle: Studies using an ocean biogeochemical general circulation model, *Global*  
1116 *Biogeochem. Cycles*, 11(4), 599–612, doi:10.1029/97GB02301, 1997.

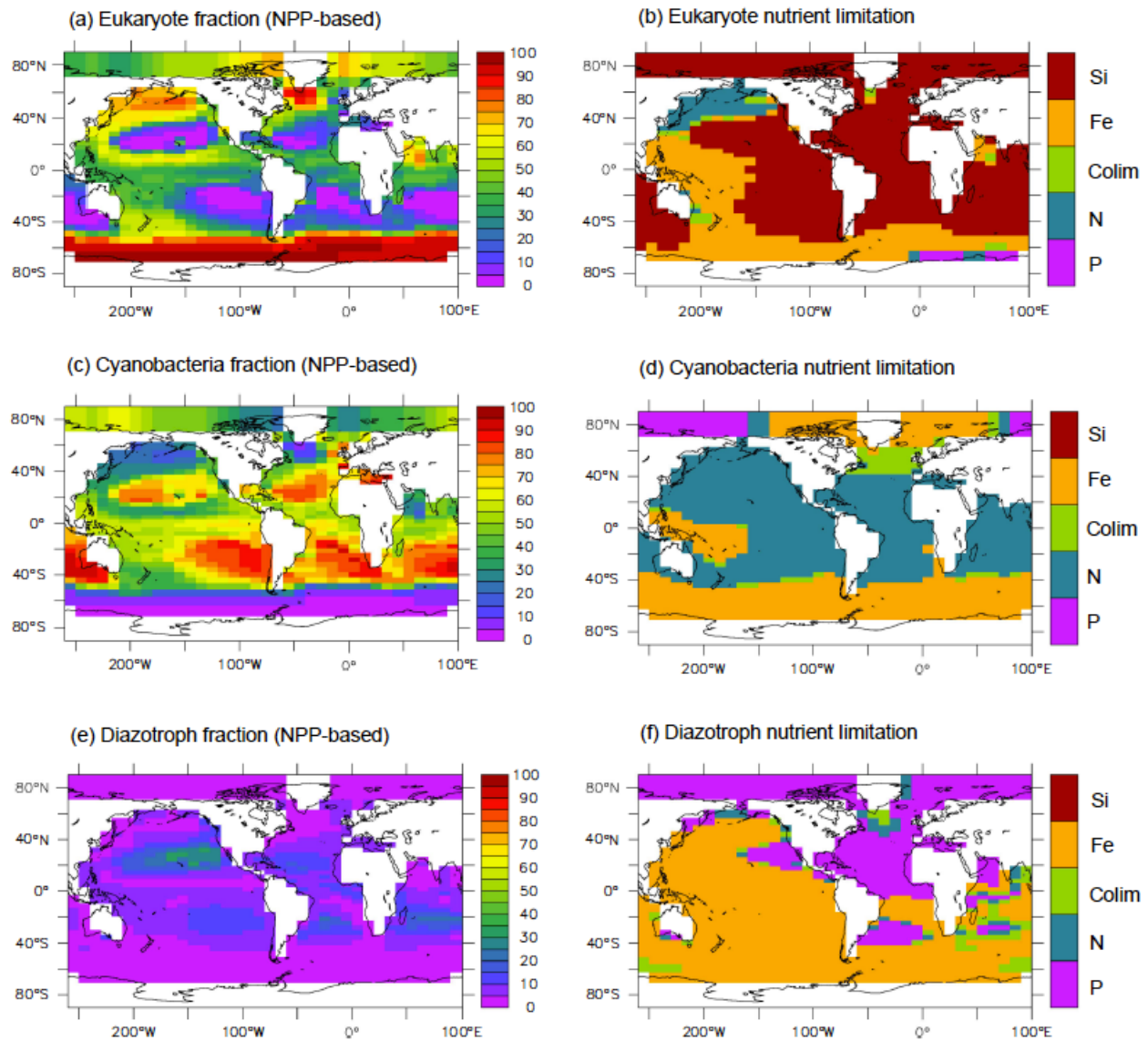
1117 Yamanaka, Y., Yoshie, N., Fujii, M., Aita, M. N. and Kishi, M. J.: An Ecosystem Model Coupled  
1118 with Nitrogen-Silicon-Carbon Cycles Applied to Station A7 in the Northwestern Pacific,  
1119 *J. Oceanogr.*, 60(2), 227–241, doi:10.1023/B:JOCE.0000038329.91976.7d, 2004.

1120 Zickfeld, K., Eby, M., Weaver, A. J., Alexander, K., Crespin, E., Edwards, N. R., Eliseev, A. V.,  
1121 Feulner, G., Fichefet, T., Forest, C. E., Friedlingstein, P., Goosse, H., Holden, P. B., Joos, F.,  
1122 Kawamiya, M., Kicklighter, D., Kienert, H., Matsumoto, K., Mokhov, I. I., Monier, E.,  
1123 Olsen, S. M., Pedersen, J. O. P., Perrette, M., Philippon-Berthier, G., Ridgwell, A.,  
1124 Schlosser, A., Von Deimling, T. S., Shaffer, G., Sokolov, A., Spahni, R., Steinacher, M.,  
1125 Tachiiri, K., Tokos, K. S., Yoshimori, M., Zeng, N. and Zhao, F.: Long-Term climate  
1126 change commitment and reversibility: An EMIC intercomparison, *J. Clim.*, 26(16),  
1127 5782–5809, doi:10.1175/JCLI-D-12-00584.1, 2013.

1128

1129





1141

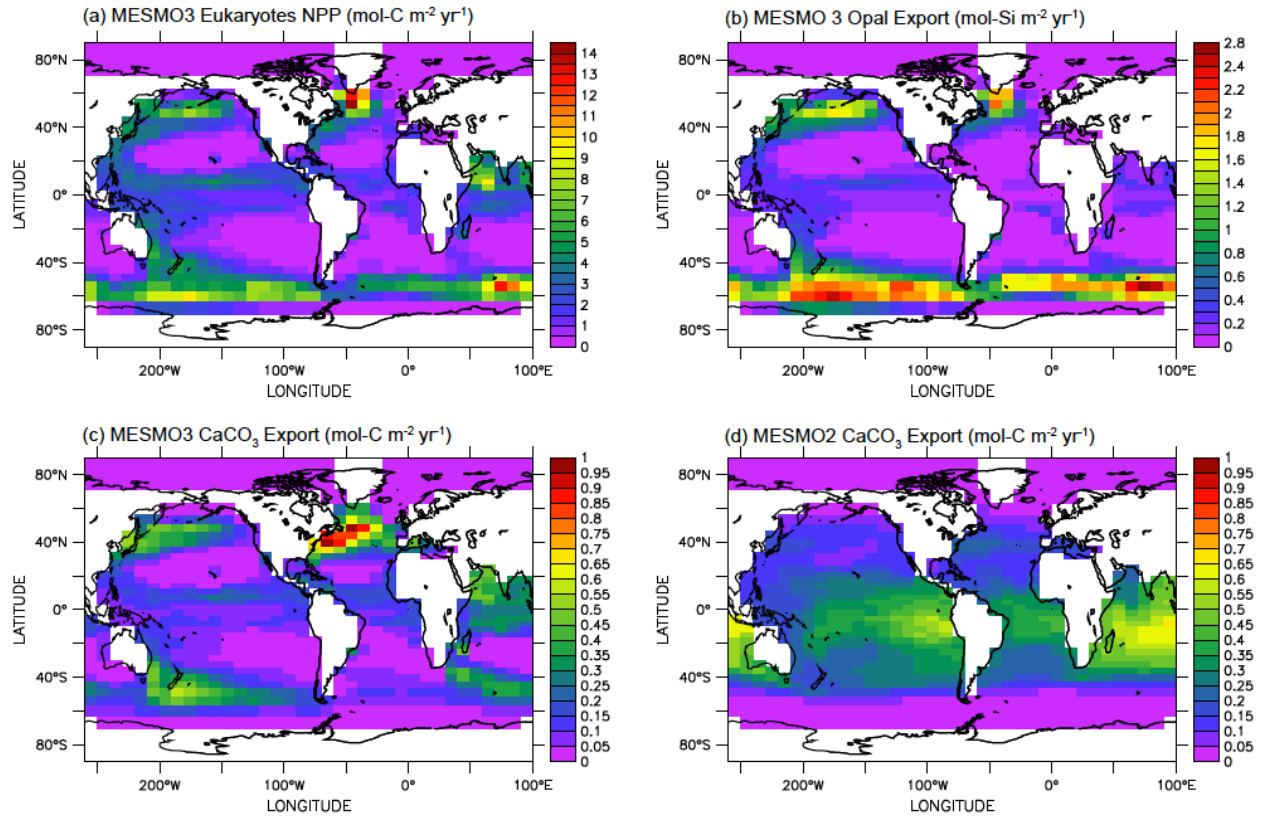
1142 **Figure 2.** NPP-based surface phytoplankton functional type (PFT) abundance and nutrient

1143 limitation in MESMO 3. Fractional abundance and nutrient limitation for eukaryotes (a, b),

1144 cyanobacteria (c, d), and diazotrophs (e, f).

1145

1146



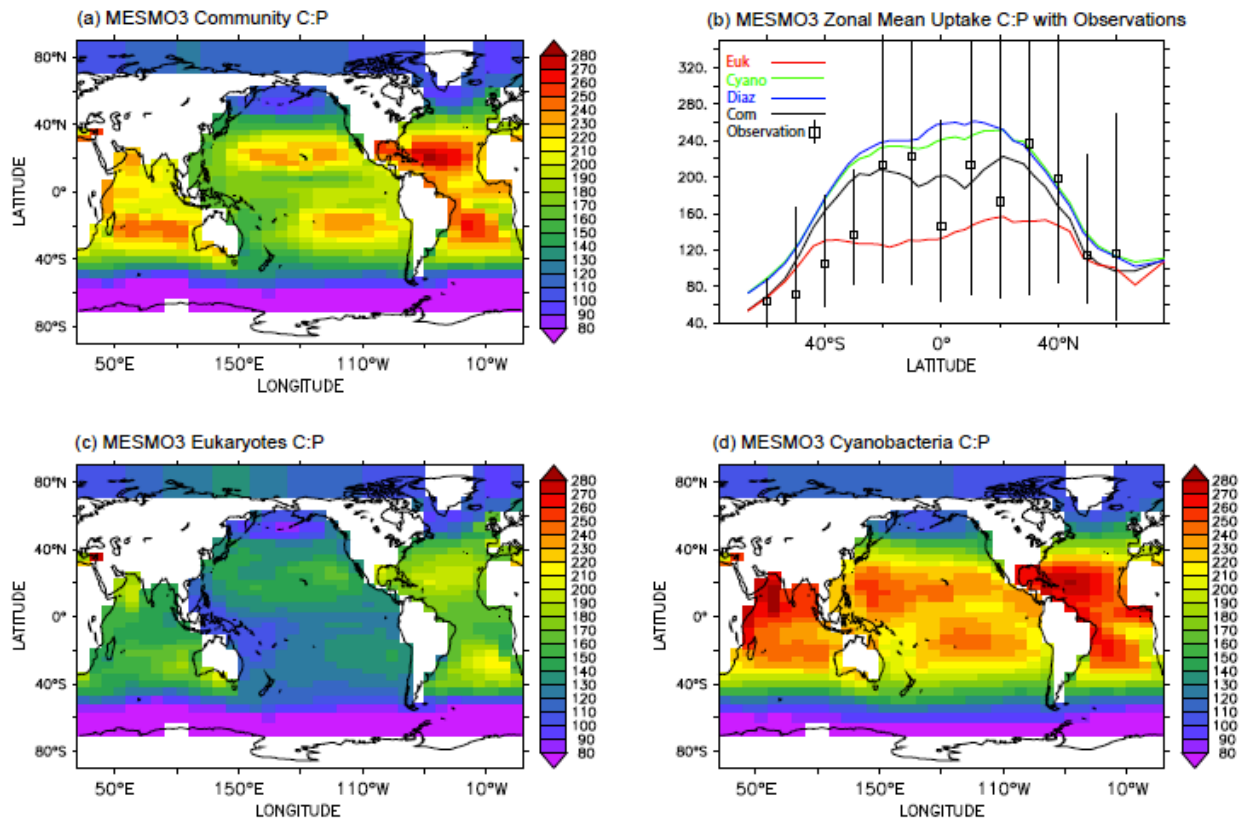
1147

1148 **Figure 3.** Eukaryote production in MESMO 3 and CaCO<sub>3</sub> export in MESMO 2. In MESMO 3,  
 1149 eukaryote NPP (a) is linked to both opal export (b) and CaCO<sub>3</sub> export (c) but the two export  
 1150 productions are differentiated by the residual nitrate potential growth (RNPG). Compare  
 1151 CaCO<sub>3</sub> export in MESMO 3 (c) to MESMO 2 (d). Unit = mol m<sup>-2</sup> year<sup>-1</sup>.

1152



1153

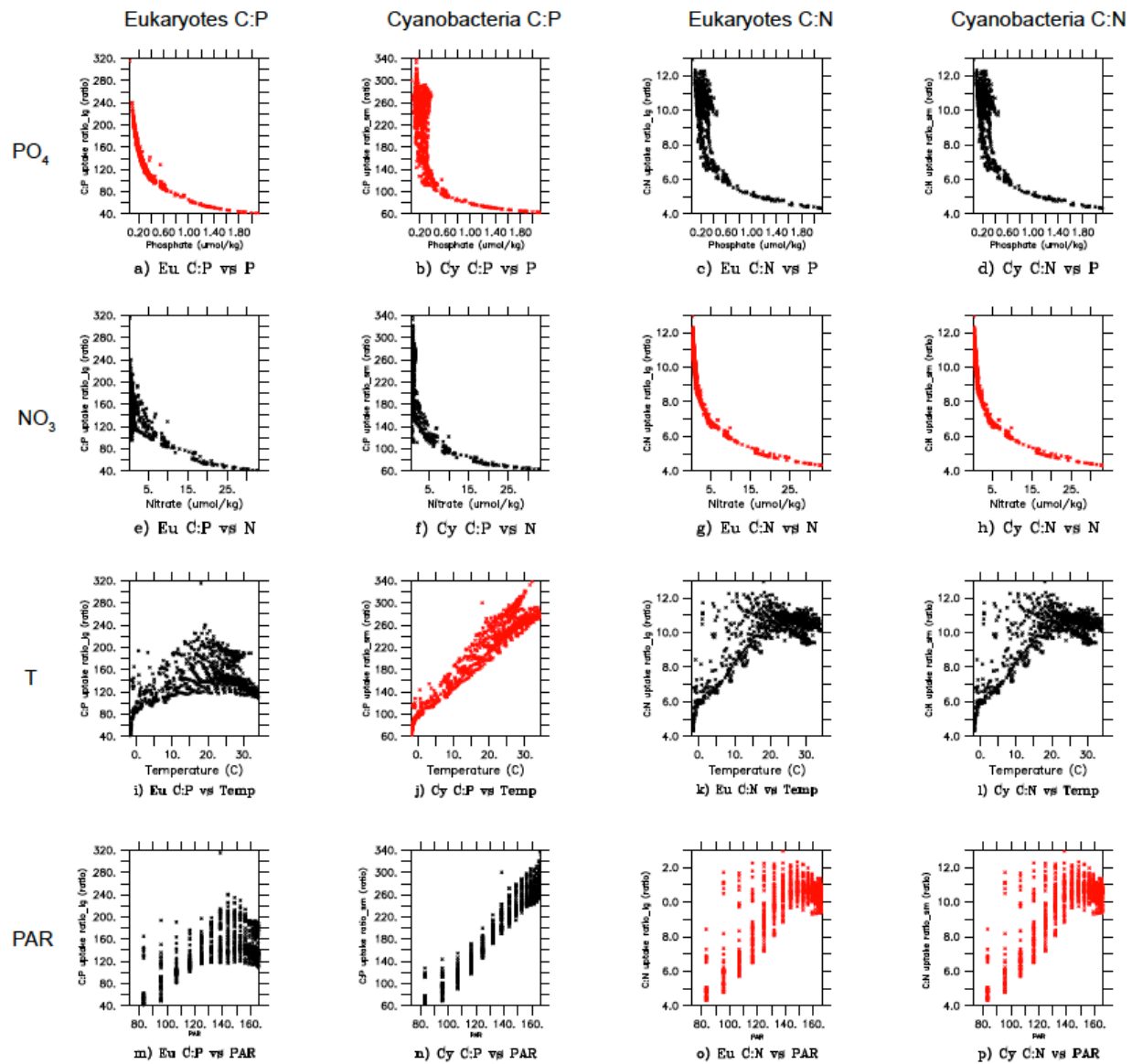


1154

1155 **Figure 4.** Uptake C:P ratio in the top 100 m in MESMO 3: (a) phytoplankton community C:P,  
1156 (b) zonal mean C:P of all three PFTs and phytoplankton community, (c) eukaryote C:P, and  
1157 (d) cyanobacteria C:P. The colors in (b) indicate: black = community C:P, red = eukaryote  
1158 C:P, green = cyanobacteria C:P, and blue = diazotroph C:P. Also, (b) shows the range of  
1159 observed C:P ratio binned by latitude (Martiny et al., 2013).

1160

1161



1162

1163 **Figure 5.** Scatter plots of surface ocean eukaryote and cyanobacteria C:P and C:N vs.

1164 environmental drivers in MESMO 3. Columns: 1 = eukaryote C:P, 2 = cyanobacteria C:P, 3 =

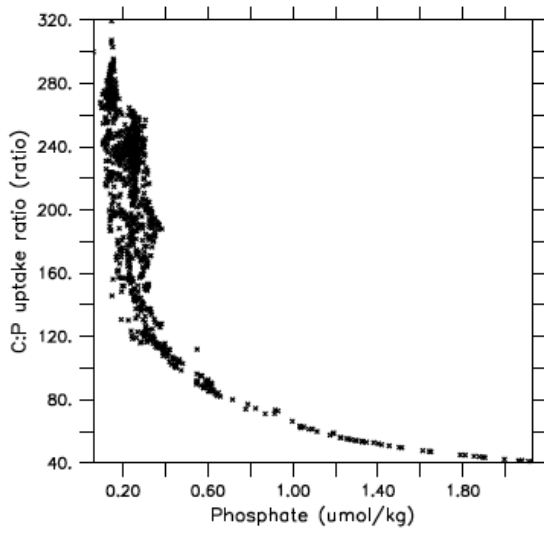
1165 eukaryote C:N, and 4 = cyanobacteria C:N. Rows: 1 = PO<sub>4</sub>, 2 = NO<sub>3</sub>, 3 = temperature, and 4 =

1166 PAR. Red indicates causal relationship according to the power law formulation of flexible

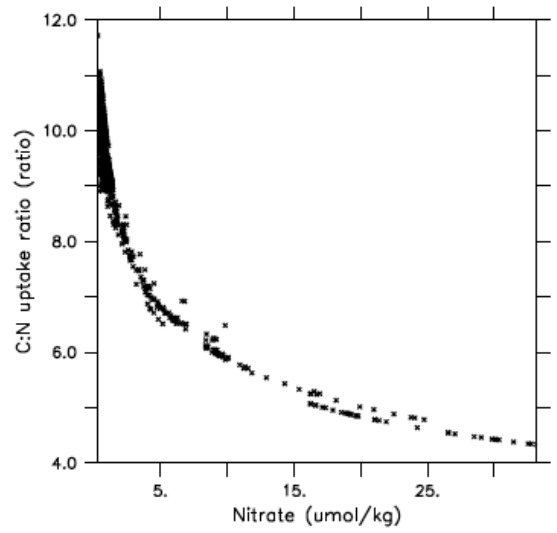
1167 C:N:P ratio. PAR = photosynthetically active radiation in W m<sup>-2</sup>.

1168

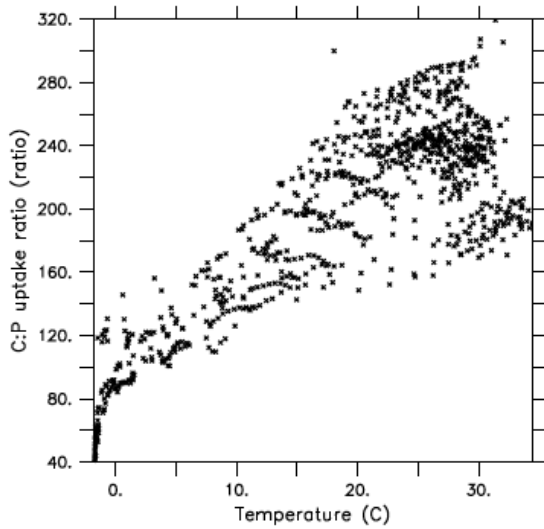
1169



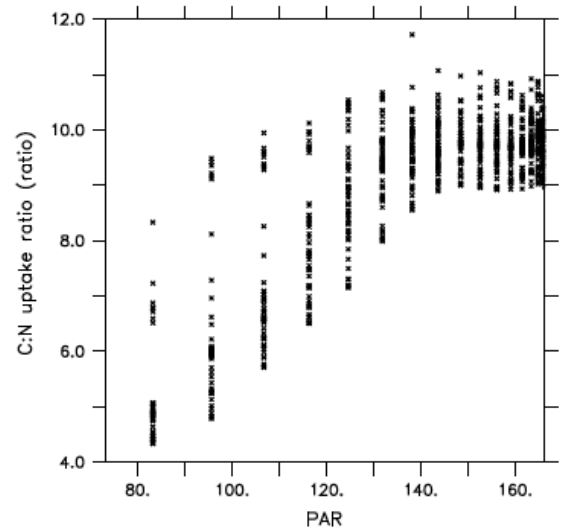
com C:P vs P



com C:N vs N



com C:P vs Temp



com C:N vs PAR

1170

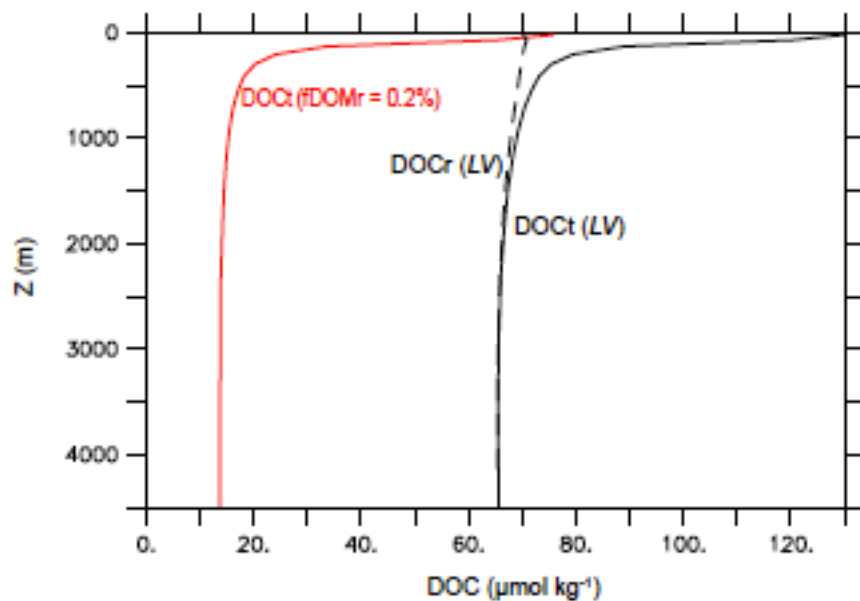
1171 **Figure 6.** Scatter plots of surface ocean community C:P and C:N vs environmental drivers in

1172 MESMO 3.

1173

1174

1175



1176

1177

1178

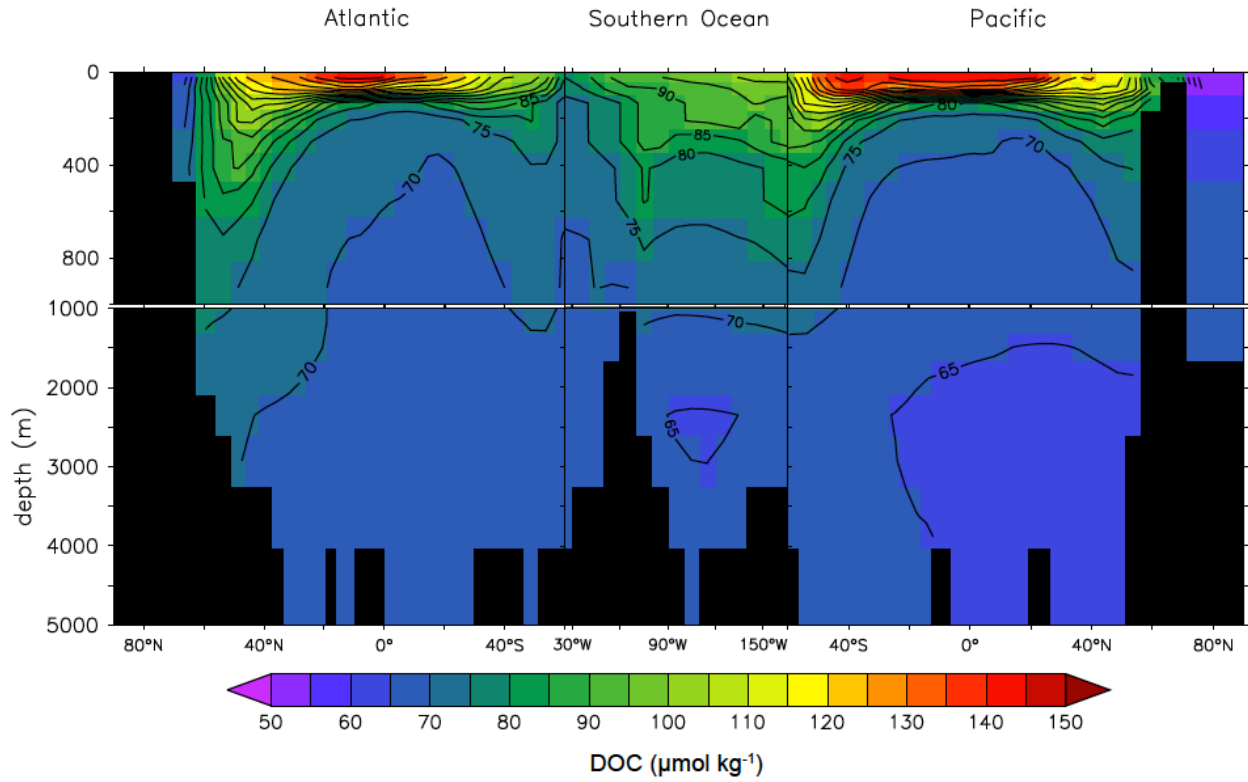
1179

1180

1181

**Figure 7.** Global mean

vertical profiles of DOC from the DOM<sub>R</sub>-enabled MESMO 3. DOC<sub>t</sub> (DOC<sub>sl</sub>+DOC<sub>r</sub>, black line) and DOC<sub>r</sub> (black dashed line) from the LV run (Experiment 210310m). Red line is DOC<sub>t</sub> after reducing fDOM<sub>r</sub> from 1% in LV to 0.2% (Experiment 210310o). Unit = μmol kg<sup>-1</sup>.



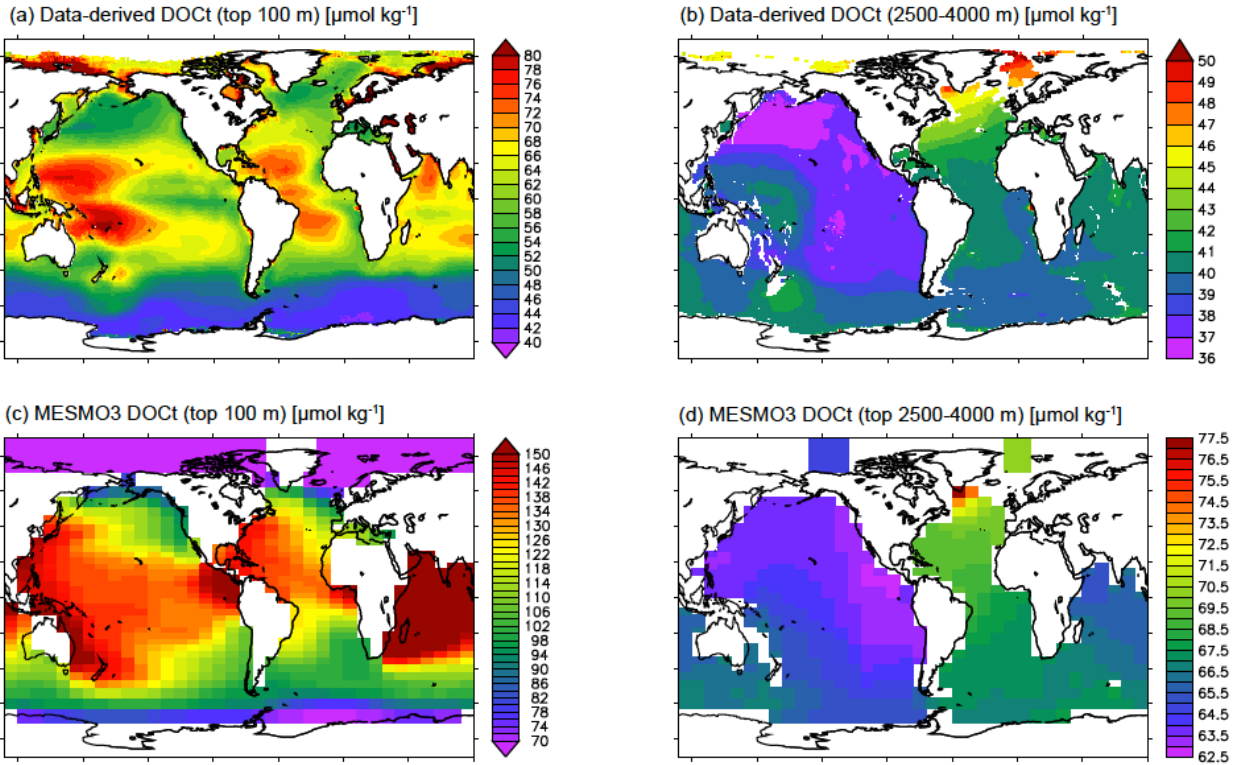
1182

1183 **Figure 8.** Global depth-latitude transect of  $\text{DOC}_t$  from the  $\text{DOM}_R$ -enabled MESMO 3 LV run.

1184 Transects are N-S along  $25^\circ\text{W}$  in the Atlantic, E-W along  $60^\circ\text{S}$  in the Southern Ocean, and N-  
 1185 S along  $165^\circ\text{E}$  in the Pacific. Unit =  $\mu\text{mol kg}^{-1}$ .

1186

1187

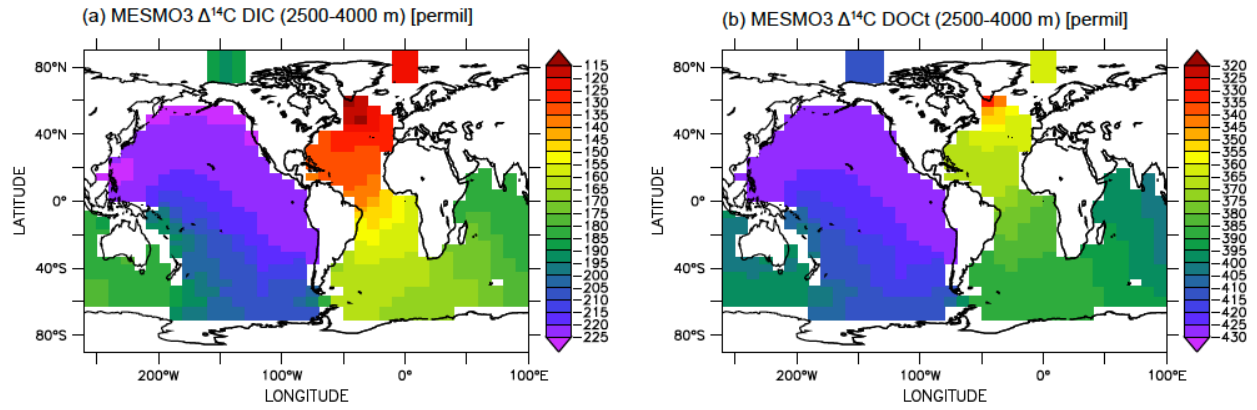


1188

1189 **Figure 9.** Assessment of surface and deep ocean  $\text{DOC}_t$  from the  $\text{DOM}_R$ -enabled MESMO 3 *LV*  
 1190 run. Data-derived  $\text{DOC}_t$  distributions in the top 100 m (a) and 2500-4000 m (b). Model-  
 1191 simulated  $\text{DOC}_t$  distributions in the top 100 m (c) and 2500-4000 m (d). Date-derived  $\text{DOC}_t$   
 1192 are from Roshan and DeVries (Roshan and DeVries, 2017). Unit =  $\mu\text{mol kg}^{-1}$ .

1193

1194



1195

1196 **Figure 10.**  $\Delta^{14}\text{C}$  of deep ocean DIC (a) and  $\text{DOC}_t$  (b) from the  $\text{DOM}_R$ -enabled MESMO 3 *LV*  
 1197 run. Vertical average over 2500-4000 m water depth. Unit = ‰.

1198

1199